ACS Catalysis

pubs.acs.org/acscatalysis

Research Article

Selective Butene Formation in Direct Ethanol-to-C_{3+}-Olefin Valorization over Zn−Y/Beta and Single-Atom Alloy Composite Catalysts Using In Situ-Generated Hydrogen

Michael J. Cordon, Junyan Zhang, Stephen C. Purdy, Evan C. Wegener, Kinga A. Unocic, Lawrence F. Allard, Mingxia Zhou, Rajeev S. Assary, Jeffrey T. Miller, Theodore R. Krause, Fan Lin, Huamin Wang, A. Jeremy Kropf, Ce Yang, Dongxia Liu, and Zhenglong Li*

Cite This: *ACS Catal.* 2021, 11, 7193−7209

Read Online

ACCESS | Metrics & More | Article Recommendations | Supporting Information

ABSTRACT: The selective production of C_{3+} olefins from renewable feedstocks, especially via C_1 and C_2 platform chemicals, is a critical challenge for obtaining economically viable low-carbon middle-distillate transportation fuels (i.e., jet and diesel). Here, we report a multifunctional catalyst system composed of Zn−Y/Beta and "single-atom" alloy (SAA) Pt−Cu/Al_2O_3, which selectively catalyzes ethanol-to-olefin (C_{3+}, ETO) valorization in the absence of cofed hydrogen, forming butenes as the primary olefin products. Beta zeolites containing predominately isolated Zn and Y metal sites catalyze ethanol upgrading steps (588 K, 3.1 kPa ethanol, ambient pressure) regardless of cofed hydrogen partial pressure (0−98.3 kPa H_2), forming butadiene as the primary product (60% selectivity at an 87% conversion). The Zn−Y/Beta catalyst possesses site-isolated Zn and Y Lewis acid sites (at ∼7 wt % Y) and Brønsted acidic Y sites, the latter of which have been previously uncharacterized. A secondary bed of SAA Pt−Cu/Al_2O_3 selectively hydrogenates butadiene to butene isomers at a consistent reaction temperature using hydrogen generated *in situ* from ethanol to butadiene (ETB) conversion. This unique hydrogenation reactivity at near-stoichiometric hydrogen and butadiene partial pressures is not observed over monometallic Pt or Cu catalysts, highlighting these operating conditions as a critical SAA catalyst application area for conjugated diene selective hydrogenation at high reaction temperatures (>573 K) and low H_2/diene ratios (e.g., 1:1). Single-bed steady-state selective hydrogenation rates, associated apparent hydrogen and butadiene reaction orders, and density functional theory (DFT) calculations of the Horiuti−Polanyi reaction mechanisms indicate that the unique butadiene selective hydrogenation reactivity over SAA Pt−Cu/Al_2O_3 reflects lower hydrogen scission barriers relative to monometallic Cu surfaces and limited butene binding energies relative to monometallic Pt surfaces. DFT calculations further indicate the preferential desorption of butene isomers over SAA Pt−Cu(111) and Cu(111) surfaces, while Pt(111) surfaces favor subsequent butene hydrogenation reactions to form butane over butene desorption events. Under operating conditions without hydrogen cofeeding, this combination of Zn−Y/Beta and SAA Pt−Cu catalysts can selectively form butenes (65% butenes, 78% C_{3+} selectivity at 94% conversion) and avoid butane formation using only *in situ*-generated hydrogen, avoiding costly hydrogen cofeeding requirements that hinder many renewable energy processes.

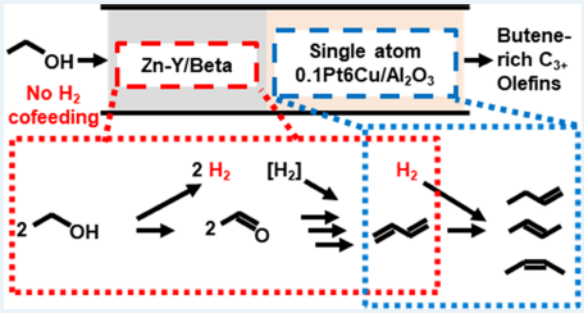

KEYWORDS: *ethanol, butenes, butadiene, selective hydrogenation, catalysis, single-atom alloy, zeolite*

1. INTRODUCTION

Efficient catalytic upgrading of renewable feedstocks into carbon-neutral transportation fuels remains critically important for combating CO_2 emissions, especially for producing long-chain (C_{8+}) hydrocarbons required for aviation and heavy-duty diesel fuels. Bioethanol is a widely produced renewable feedstock (∼86 million tons per year worldwide in 2018[1]) that can be valorized into key short-chain (C_3−C_6) olefin intermediates (e.g., propene,[2] 1-butene, isobutene[3]), a class of critical precursors for oligomerization into middle-distillate-range hydrocarbons[4] and commodity chemical production.[5] Direct conversion of ethanol to C_{3+} olefins is typically accomplished over either Brønsted acid zeolites[6,7] or metal oxides[8−10] with limited olefin selectivities due to the formation of aromatics and paraffins,[11−13] ethylene, oxygenates, or other side products including CO_2.[14,15] Therefore, a strong need remains for an approach to selective C_{3+} olefin production for

Received: March 11, 2021
Revised: April 29, 2021
Published: June 4, 2021

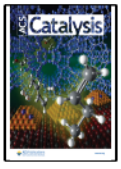

https://doi.org/10.1021/acscatal.1c01136
ACS Catal. 2021, 11, 7193−7209

Scheme 1. Proposed ETO Reaction Pathway Composed of ETB and Subsequent Butadiene Selective Hydrogenation to Form Butene Isomers[a]

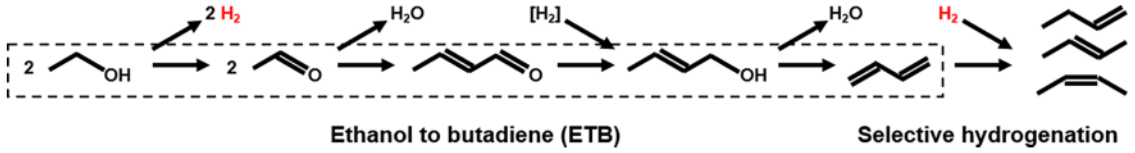

[a]H_2 production and consumption events are highlighted in red. An additional ethanol provides the hydrogen source for the MPV reduction of crotonaldehyde.

Scheme 2. Two-Bed Reactor Setup Composed of Independent ETB and Selective Hydrogenation (SH) Catalysts[a]

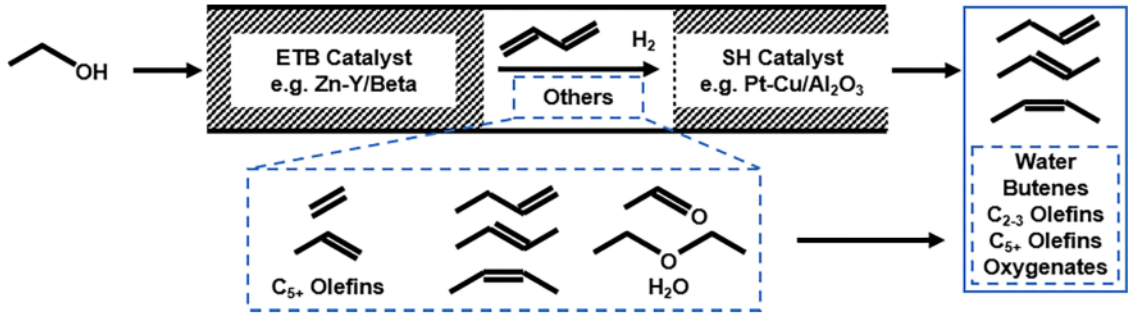

[a]Catalyst beds are in physical contact during reaction, with the distance here shown only to highlight key intermediates passing between catalyst beds. Components labeled as "others" are products that are not typically observed to change significantly by the choice of SH catalyst in the absence of hydrogen cofeeding. Single-bed ethanol valorization studies were performed over Zn−Y/Beta without an SH catalyst (vide infra Section 3.1), and single-bed selective hydrogenation reactions were performed without an ETB catalyst (vide infra Section 3.3).

economically viable liquid renewable fuel generation without significant carbon losses, especially since carbon conversion efficiency is a primary cost driver for renewable fuel production.[16]

Ethanol conversion to 1,3-butadiene (ETB) is an economically attractive reaction for selectively generating renewable C_4 monomers that can avoid the above-mentioned side product formation[17] and can serve as an important step toward the synthesis of butene-rich olefins. Despite debates about the specific mechanistic details, the general reaction network of ETB (Scheme 1) consists of ethanol dehydrogenation, aldol condensation, Meerwein−Ponndorf−Verley (MPV) reduction, and dehydration to form 1,3-butadiene (butadiene, BD).[18−20] For an ideal reaction resulting in perfect ethanol-to-butadiene selectivity, stoichiometric amounts of butadiene and hydrogen are formed due to hydrogen generated from ethanol dehydrogenation (Scheme 1). However, butadiene is not a preferred C_4 olefin for middle-distillate fuel generation due to its tendency for increased coke formation.[21−24] Therefore, one attractive approach is to directly utilize this *in situ*-generated hydrogen for the selective hydrogenation of butadiene to butenes without requiring cofed hydrogen, providing a single-reactor approach for converting ethanol into a butene-rich olefin stream. Such ethanol-to-C_{3+}-olefin (ETO) valorization without external hydrogen has not been reported in the literature and offers the benefits of avoiding the operating and capital costs associated with hydrogen purchase, storage, downstream separation, and recycling. The grand challenge of this ETO pathway is designing catalytic materials with active sites for both high ETB reactivity and high butadiene selective hydrogenation reactivity while mitigating butene hydrogenation to butanes under stoichiometric hydrogen and butadiene partial pressures and ETB reaction conditions (e.g., 573−673 K).[25−27]

ETB catalysts typically possess multiple kinetically relevant active sites for dehydrogenation and aldol condensation steps, which are often derived from transition-metal and oxide pairings[28] such as metal-promoted MgO/SiO_2.[29−32] Zeolites have also shown promising ETB reactivity through the combination of Lewis acid sites formed through the isomorphous substitution of framework Si centers with M^{4+} or M^{5+} heteroatoms and transition-metal sites (e.g., Ag/Zr-Beta,[33] Cu-Ta/Beta,[34] Zn/Hf-MFI[35]), utilizing favorable confinement effects in conjunction with dispersed active sites to improve desired product selectivities. Recently, rare-earth metals (e.g., Y) operating as Lewis acid sites within Beta zeolite microporous environments have been investigated as aldol condensation active sites and can catalyze the ETB reaction pathway (603 K) when combined with transition metals (e.g., Zn).[36] This suggests Zn−Y/Beta as an effective ETB catalyst within the larger ETO reaction pathway[19] to produce near-stoichiometric butadiene and hydrogen partial pressures for further catalyst upgrading.

Using butadiene as an intermediate, the ETO pathway requires the selective hydrogenation of butadiene to form butene. Butadiene selective hydrogenation reaction is generally studied at lower temperatures (<423 K) and is often performed with excessive amounts of hydrogen (H_2/BD > 15).[37] Butane formation can be observed[37,38] even at such mild reaction temperatures and with H_2/BD ratios similar to those observed in naphtha steam-cracking applications,[39] situations where the selective hydrogenation of acetylene to ethylene or butadiene to butenes is necessary prior to downstream operations. Traditional butadiene selective hydrogenation catalysts include Cu/SiO_2,[40] Pd/Al_2O_3,[41] and $Pt\text{-}Ni/Al_2O_3$,[42] while "single-atom alloy" (SAA)-supported metal catalysts composed of dilute solid solutions of precious metals (e.g., Pd or Pt) within transition-metal nanoparticles (e.g., Cu) have

https://doi.org/10.1021/acscatal.1c01136
ACS Catal. 2021, 11, 7193−7209

recently been studied as relevant selective hydrogenation catalysts.[37,43,44] Low-temperature (<423 K) butadiene selective hydrogenation reactivity over Pt−Cu SAA catalysts has been qualitatively correlated with the formation of hydrogen islands around Pt centers through hydrogen adsorption, scission, and subsequent adatom diffusion to proximal Cu centers;[37] however, their applicability for higher temperatures has not been investigated and particularly not for near-stoichiometric hydrogen and butadiene partial pressures.

Here, this ETO reaction pathway is investigated for the first time using a two-bed reactor setup containing Zn−Y/Beta and Pt- and/or Cu-containing supported metal catalysts (Scheme 2) to catalyze ethanol to butadiene and subsequent butadiene selective hydrogenation, respectively, generating C_{3+} olefins from ethanol alone without external hydrogen feeding. Both catalysts are individually characterized using a suite of spectroscopy and microscopy techniques including X-ray absorption spectroscopy (XAS), pyridine-adsorbed transmission IR spectroscopy, and scanning transmission electron microscopy (STEM). Catalysts are tested in both single-bed and two-bed configurations (588 K; Scheme 2) as a function of cofed hydrogen partial pressures (0−98.3 kPa). Steady-state reaction rates, apparent reaction order measurements, and density functional theory (DFT) calculations are employed to compare selective hydrogenation catalysts (SAA 0.1Pt6Cu/Al_2O_3, 0.1Pt/Al_2O_3, 2Pt/Al_2O_3, and 6Cu/Al_2O_3) and investigate the unique kinetic capabilities of Pt−Cu ensemble sites under near-stoichiometric hydrogen concentrations desired for ideal ETO operations and negligible butane formation. These combined experimental and computational results indicate the ETO catalytic potential of the composite catalyst composed of Zn−Y/Beta and SAA 0.1Pt6Cu/Al_2O_3 utilizing stoichiometric hydrogen partial pressures formed *in situ* and eliminating costly hydrogen cofeeding and corresponding downstream hydrogen separation and recycle steps in the middle-distillate-range hydrocarbon generation processes.

2. EXPERIMENTAL METHODS

2.1. Catalyst Synthesis. Dealuminated Beta (deAl-Beta) was obtained using a previously reported procedure,[45] with details shown in Section S.1.1. Zn−Y/Beta, Zn/Beta, and Y/Beta samples were synthesized from the deAl-Beta support via solid-state grinding. In a typical Zn−Y/Beta synthesis, 0.091 g of zinc nitrate hexahydrate (Sigma-Aldrich, 97%) and 0.345 g of yttrium nitrate hexahydrate (Sigma-Aldrich, 97%) precursors were ground with deAl-Beta for 0.25 h. The resulting solids were heated in a tube furnace to 823 K (0.0167 K s^{-1}) under airflow (10 cm^3 s^{-1} (g catalyst)$^{-1}$). Pt- and Cu-containing supported metal catalysts were synthesized through incipient wetness impregnation onto a γ-alumina (Al_2O_3) support (Sinopharm Chemical Reagent Co., Ltd., 98.0%), with details reported in Section S.1.1.

2.2. Catalyst Characterization. Powder X-ray diffraction (XRD) patterns were measured on a PANalytical X-ray diffractometer using a Cu Kα source (λ = 0.1542 nm, 45 kV, 40 mA). Diffraction patterns were collected from 4 to 40° at a step size of 0.025° and a scan rate of 0.04° s^{-1}. N_2 adsorption isotherms (77 K) were collected using a Quantachrome Autosorb iQ with detailed analysis information reported in Section S.1.2. Bulk elemental compositions were measured via inductively coupled plasma atomic emission spectroscopy (ICP-AES) performed at Galbraith Laboratories, Inc. Aberration-corrected high-angle annular dark-field imaging from scanning transmission electron microscopy (HAADF-STEM) was performed to probe bulk metal distributions for both Zn−Y/Beta and Al_2O_3-supported metal catalysts with characterization details reported in Section S.1.2. Transmission IR spectra were collected on Zn- and Y-containing zeolite samples after pyridine adsorption, and the measurement details are also reported in Section S.1.2.

XAS experiments were performed in transmission mode at the Zn and Y K edges (9.659 and 17.038 keV, respectively, for zeolite samples) and at the Pt L_3 edge and Cu K edge (11.564 and 8.9789 keV, respectively, for supported metal catalysts) on the Materials Research Collaborative Access Team (MR-CAT) bending magnet beamline at the Advanced Photon Source at Argonne National Laboratory. For samples with low Pt loading, the Pt L_3 edge XAS experiments were performed in fluorescence mode at the MR-CAT insertion device line, 10-ID. Detailed sample pretreatment, measurement procedures, and data analysis methodologies are reported in Section S.1.2.

2.3. Gas-Phase Ethanol Conversion Studies. High ethanol conversions for the two-bed reactor setup or single-bed Zn−Y/Beta were measured using a vertically aligned tubular quartz reactor (0.5″ OD) under ambient pressures. Catalysts were pelletized, crushed, and sieved to retain particles within 125 and 180 μm prior to being loaded into the reactor (Scheme 2). Catalyst beds were placed between quartz wool beds (Chemglass, 8−15 μm) with typical bed masses of 0.250 g for Zn−Y/Beta in the first bed and 0.168 g of the desired selective hydrogenation catalyst in the second bed, unless otherwise stated. For single-bed operation, 0.250 g of Zn−Y/Beta was loaded. Constant catalyst bed temperatures were measured using a K-type thermocouple (Omega) positioned within the first catalyst bed. Catalysts were heated to 673 K (0.0833 K s^{-1}) in a flowing He (0.33 cm^3 s^{-1}, Airgas, UHP, >99.999%) for 1 h, switched to pure H_2 flow (0.42 cm^3 s^{-1}, Airgas, UHP, >99.999%) at 673 K for 0.5 h, and then switched back to flowing He while cooling to 588 K. Catalyst beds were then exposed to relevant H_2 and He gas flow conditions (0.48 cm^3 s^{-1}, P_{H_2} = 0−101.3 kPa with balance He, preheated to 453 K). Liquid ethanol (EMD Millipore, >99%) was fed into the heated gas mixture via a syringe pump (KD Scientific Legato 180) and vaporized prior to interacting with the catalyst beds. No background reactions were detectable using only quartz wool within the reactor. Products were separated and analyzed via gas chromatography (Agilent 7820A) using a HP-PLOT-Q column (30 m, 0.32 mm diameter, 20 μm film) and both a flame ionization detector and a thermal conductivity detector. Product identification was performed using a gas chromatograph (GC, Agilent 6850) and mass spectrometer (Agilent 5975C) with known standards. The carbon balance for all of the reactions is typically 92−96%. Definitions of ethanol conversions, product yields, and selectivities are reported in Section S.1.3.

Reaction rates for Zn- and Y-containing samples were measured in the same setup as the high conversion experiments. Catalyst weight, ethanol flow rates, and carrier gas flow rates were adjusted to maintain a differential conversion regime with ethanol conversion <5%. Typically, 0.05 g of catalyst was pelletized, crushed, and sieved to retain particles within 125 and 180 μm and then diluted with 0.80 g silicon carbide (SiC, Alfa Aesar, 120 grit). Ethanol flow rates were controlled via a syringe pump (1.07 mL h^{-1}) into Ar (1.67 cm^3 s^{-1}, 588 K, 163 kPa total pressure).

https://doi.org/10.1021/acscatal.1c01136
ACS Catal. 2021, 11, 7193−7209

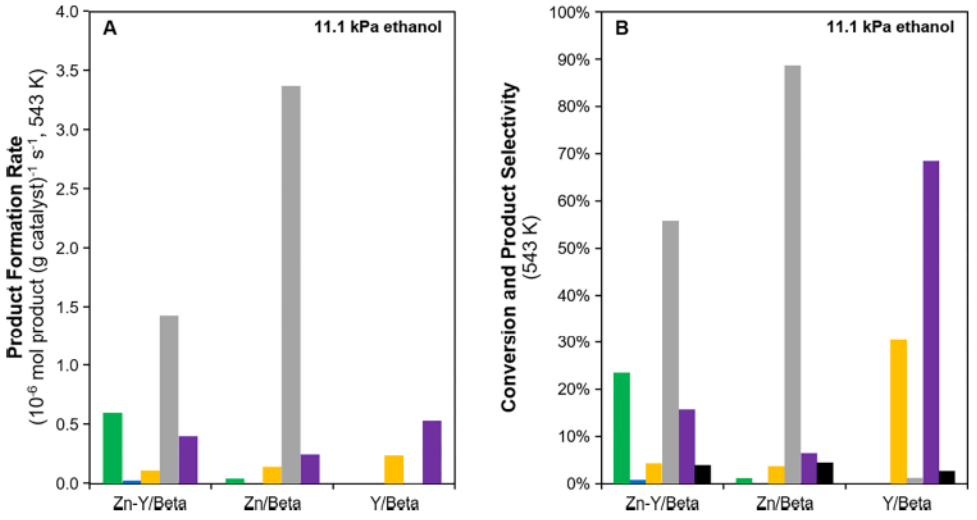

Figure 1. (A) Product formation rates from ethanol valorization (11.1 kPa ethanol in balance Ar, 163 kPa total pressure, 543 K, WSHV = 15.9 h^{-1} over Zn/Beta and Zn−Y/Beta and 8.0 h^{-1} over Y/Beta, <5% conversion) to form butadiene (green), butenes (blue), ethylene (orange), acetaldehyde (gray), and diethyl ether (purple) and (B) associated conversions (black) and product selectivities over Zn−Y/Beta, Zn/Beta, and Y/Beta catalysts.

2.4. Butadiene Selective Hydrogenation Kinetic Studies. Butadiene selective hydrogenation rates were measured using a similar reactor setup as used for ethanol upgrading but with only a single catalyst bed. Typically, 0.05 g of catalyst (pelletized, crushed, and sieved to 125−180 μm) was mixed with 0.70 g of SiC (Alfa Aesar, 120 grit) prior to being loaded into the reactor between two quartz wool plugs. Catalyst beds were pretreated to 673 K (0.0833 K s^{-1}) in 10% H_2 in balance Ar (UHP, Airgas, >99.999%, 0.83 cm^3 s^{-1}) for 1 h prior to cooling to 588 K. Gas flow rates of H_2 and Ar were adjusted and butadiene (BD, Airgas, 3%, balance N_2) and a methane internal standard (CH_4, Airgas, 1%, balance Ar) were introduced to obtain a reference condition (F_{total} = 1.67 cm^3 s^{-1}, P_{H_2} = 1.51 kPa, P_{BD} = 1.51 kPa, P_{CH_4} = 0.20 kPa). Transient behavior was observed for at least 12−18 h over each selective hydrogenation catalyst to provide sufficient data to fit initial and steady-state rate measurements at initial and near-infinite times on stream. Initial and steady-state rates represent modeled regressions of transient profiles from a two-site model with better fitting results than a one-site model as expected for complex materials with multiple active site configurations. Reaction orders reflect rate measurements after catalyst stabilization at H_2 partial pressures between 0.76 and 2.99 kPa and butadiene partial pressures between 0.51 and 2.53 kPa, with reported rates reflecting the average of 1 h of data collection (3 data points, <5% deactivation during kinetic measurements at each H_2/BD ratio). Flow compositions were returned to the initial reference condition after each reaction order measurement to ensure the reclamation of steady-state reference rates. Product quantification was performed through an identical procedure to the ethanol conversion setup prior to normalization by the methane internal standard.

2.5. DFT Methods. All of the calculations were carried out using the Vienna ab initio simulation package (VASP)[46,47] with the van der Waals interaction (DFT-D3 correction)[48,49] included. Exchange−correlation energies were described using the generalized gradient approximation (GGA) Perdew−Burke−Ernzerhof (PBE) functional.[50] The closed-packed (111) facet was generated to reflect a common facet in face-centered cubic transition-metal nanoparticles[51] and was represented by a five-layer slab (3 × 3). Studied surfaces include a Cu(111) surface, a Pt(111) surface, and an SAA Pt−Cu(111) surface, the latter of which reflects the substitution of a single Pt atom into the Cu(111) surface. A 20 Å vacuum was added between the two neighboring successive slabs for all of the simulated surfaces. A Monkhorst−Pack *k*-point mesh[52] of 3 × 3 × 1 (400 eV cutoff energy) was used during structure optimization, and the optimized structures were obtained when changes in force were less than 0.02 eV $Å^{-1}$. The most stable adsorption configurations reflect the lowest-energy structures from several adsorption configurations. Transition states for each reaction step were determined based on combined climbing image nudged elastic band (CI-NEB)[53] and dimer methods.[54] The vibrational frequencies of adsorbed butadiene, 1-butene, *cis*-2-butene, and *trans*-2-butene were computed on each surface to estimate the thermodynamic properties. Only the adsorbates were allowed to relax to accelerate the vibrational frequency calculations. The binding energies (BEs) of reaction intermediates, including butadiene, H_2, H adatom, 1-butene, *cis*-2-butene, and *trans*-2-butene, were calculated based on eq 1

$$BE_{A^*} = E_{A^*} - E^* - E_A \quad (1)$$

Here, BE_{A^*} is the total energy of adsorbate species A, E^* is the total energy of the clean surfaces, and E_A is the total energy of gas A (e.g., butadiene, H_2, 1-butene, *cis*-2-butene, and *trans*-2-butene). For gaseous H adatoms, the E_A was approximated as half of the total energy of H_2 gas.

3. RESULTS

3.1. Ethanol Upgrading over Bimetallic Zn−Y/Beta. X-ray diffraction patterns and micropore volumes determined from N_2 adsorption isotherms (77 K) collected on zeolite samples after metal incorporation are consistent with the Beta topology (Figures S.1 and S.2 and Table S.1). Inductively coupled plasma atomic emission spectroscopy (ICP-AES) measurements show no detectable Al presence within the Beta support (Si/Al > 1300) and therefore negligible Al Brønsted acid site densities. Zn and Y ICP-AES measurements indicate

https://doi.org/10.1021/acscatal.1c01136
ACS Catal. 2021, 11, 7193−7209

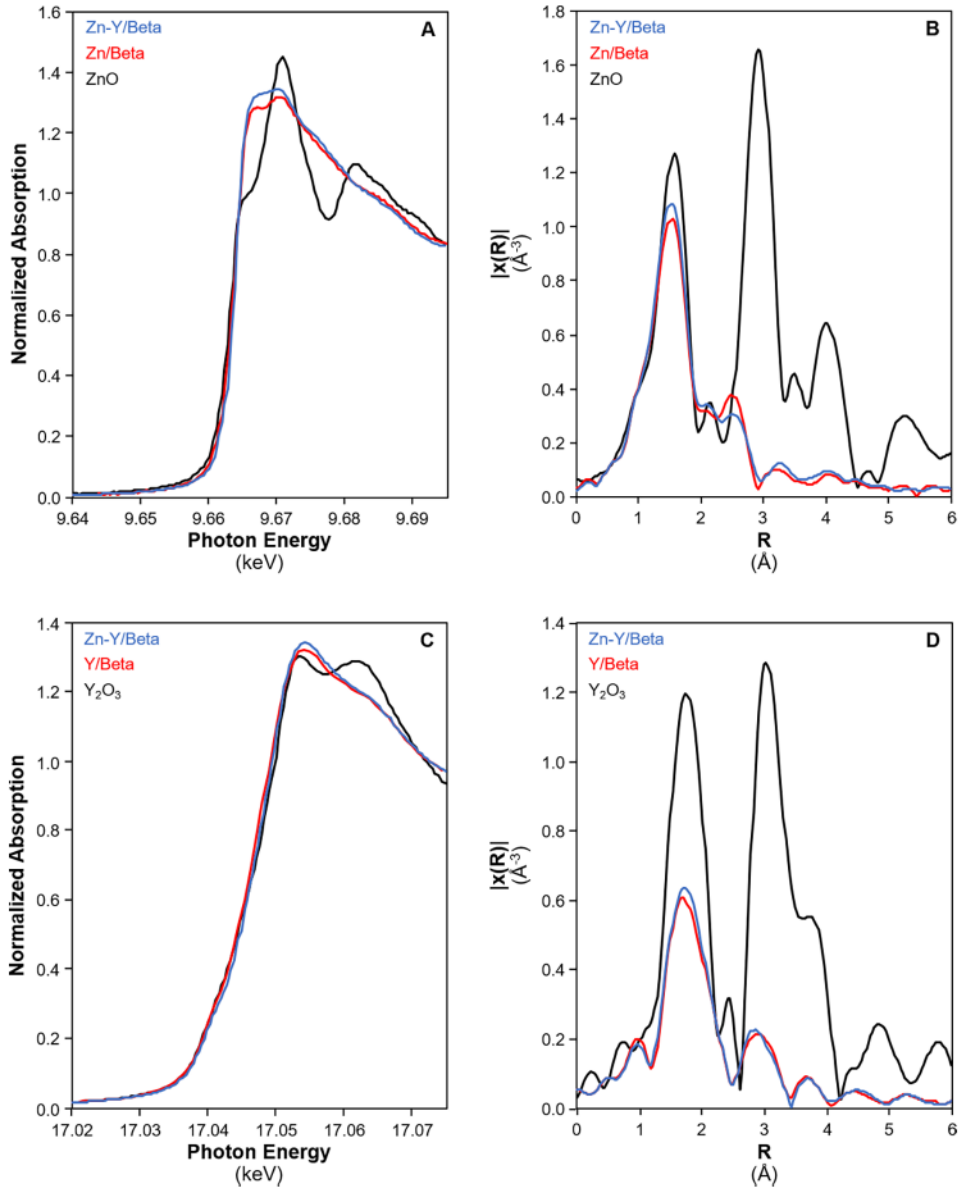

Figure 2. XAS spectra collected on Zn- and Y-containing samples after pretreatment in flowing He to 673 K, including Zn K edge XANES (A) and EXAFS (B, k^2 weightings) spectra and Y K edge XANES (C) and EXAFS (D, k^2 weightings).

bulk metal loadings of 2.0 and 7.3 wt %, respectively, on monometallic samples and are similar for Zn−Y/β (1.7 and 7.0 wt % Zn and Y, respectively; Table S.1).

Figure 1 shows ethanol conversion rates measured over Zn−Y/Beta, Zn/Beta, and Y/Beta catalysts (11.1 kPa EtOH in balance Ar, 163 kPa total pressure, 543 K, weight hourly space velocity (WHSV) = 15.9 g EtOH (g catalyst)$^{-1}$ h^{-1} over Zn/Beta and Zn−Y/Beta and WHSV = 8.0 g EtOH (g catalyst)$^{-1}$ h^{-1} over Y/Beta, <5% conversion) to probe the catalytic necessity of both Zn and Y species. Zn/Beta predominantly forms acetaldehyde, a key reactant for aldol condensation into crotonaldehyde and subsequent butadiene formation (Scheme 1). Y centers within Y/Beta yield ethylene and diethyl ether predominantly, indicating negligible dehydrogenation reactivity under these conditions and corroborating previous observations at 623 K.[19] As the incorporation of both Zn and Y centers produces quantifiable amounts of butadiene and butenes over Zn−Y/Beta, apparent ethanol dehydrogenation rates reflecting combined acetaldehyde, butadiene, and butene formation are used to compare Zn−Y/Beta and Zn/Beta. Measured dehydrogenation rates over Zn−Y/Beta and Zn/Beta are similar, normalized per gram or per mol of Zn (1.0×10^{-2} and 1.1×10^{-2} mol dehydrogenated EtOH (mol Zn)$^{-1}$ s^{-1}, respectively), which is consistent with negligible ethanol dehydrogenation reactivity over Y centers in Y/Beta (1.2×10^{-5} mol EtOH (mol Y)$^{-1}$ s^{-1}). Butadiene formation rates over Zn−Y/Beta are 13× higher than over Zn/Beta at similar Zn loadings, suggesting the catalytic need for Y sites or Zn−Y ensemble sites for catalyzing the aldol condensation, MPV reduction, and dehydration reaction network that converts two acetaldehyde molecules into butadiene.

To probe the local environment of Zn and Y centers, XAS measurements and HAADF-STEM analyses were performed on the Zn- and Y-containing zeolite samples. Figure 2 shows X-ray absorption near-edge structure (XANES) and extended X-ray absorption fine structure (EXAFS) spectra of the fresh Zn- and Y-containing samples after dehydration at 673 K (EXAFS fits and Supporting Information in Tables S.2 and S.3 and

https://doi.org/10.1021/acscatal.1c01136
ACS Catal. 2021, 11, 7193−7209

Figures S.3–S.6). At the Zn K edge, the XANES edge energies of Zn/Beta (9.6639 keV) and Zn–Y/Beta (9.6642 keV) are close to that of ZnO (9.6633 keV), indicating predominantly Zn^{2+} centers in all three materials. The Zn K edge EXAFS spectrum (Figure 2B) of ZnO shows two primary peaks centered at 1.6 and 2.9 Å (phase-uncorrected distance) reflecting Zn–O first-shell scattering and Zn–Zn second-shell scattering, respectively. A Zn–O scattering peak centered at 1.5 Å (phase-uncorrected distance) is observed in the EXAFS spectra of Zn/Beta and Zn–Y/Beta. Fitting gives coordination numbers close to 4 at a similar distance to the Zn–O bond in ZnO. Zn–Zn scattering is not observed in the EXAFS of Zn/Beta or Zn–Y/Beta, indicating that Zn centers are highly dispersed on the Beta supports and that large Zn oxide nanoparticles are absent.

At the Y K edge, the XANES edge energies of Y/Beta (17.0402 keV), Zn–Y/Beta (17.0399 keV), and Y_2O_3 (17.0402 keV) are all similar, indicating Y in the 3+ oxidation state on all three materials. The EXAFS spectrum (Figure 2D) of Y_2O_3 shows scattering from Y–O at 1.8 Å (phase-uncorrected distance) as well as two prominent peaks from 2.6 to 4.2 Å (phase-uncorrected distance), reflecting single and multiple scatterings from Y in the second and third coordination spheres. In contrast, Y/Beta and Zn–Y/Beta have a Y–O peak with much lower intensity and a small second-shell peak at a shorter distance compared to Y_2O_3. Fitting the first shell gave a coordination number of close to 4 for both catalysts with a distorted environment having two short and two long Y–O bonds. In contrast, Y_2O_3 is octahedral as reflected in a much higher Y–O peak amplitude (Figure 2D). The lack of higher Y shell peaks on Y/Beta and Zn–Y/Beta indicates the absence of significant YO_x nanoparticles occluded on the zeolite domains despite the relatively high Y loading. HAADF-STEM images of Zn–Y/Beta (Figure S.7) support the conclusions from EXAFS and show no discernible Zn or Y oxide nanoparticles, suggesting the highly dispersed nature of both Zn and Y on the zeolite support. Taken together, monometallic Zn/Beta and Y/Beta and bimetallic Zn–Y/Beta each consist of predominately isolated Zn^{2+} and Y^{3+} centers on the Beta zeolite support.

The Lewis or Brønsted acidic properties of the dispersed Zn and Y sites were probed using transmission IR. Figure 3 displays transmission IR spectra collected after pyridine saturation of Zn–Y/Beta, Zn/Beta, Y/Beta, and deAl-Beta materials. The spectrum collected after pyridine adsorption onto the deAl-Beta parent material shows only minor peaks, while adsorption onto Zn/Beta and Y/Beta gives rise to peaks at 1491 and 1575 cm^{-1} and two distinct peaks each (1452 and 1612 cm^{-1} for Zn, 1445 and 1606 cm^{-1} for Y), reflecting pyridine adsorbed onto Zn and Y sites, respectively. The four distinct peaks match peaks for pyridine adsorption onto ZnO[55] and Y_2O_3,[56] reflecting pyridine adsorbed onto Lewis acid sites. These peaks centered around 1450 and 1610 cm^{-1} and the shared peak centered at 1491 cm^{-1} reflect perturbed pyridine deformation modes upon adsorption onto Lewis acid sites,[57] while the peak centered at 1575 cm^{-1} corresponds to hydrogen-bonded pyridine.[58] Peaks reflecting pyridine adsorption onto Zn sites in Zn/Beta match previous observations of pyridine-bound Lewis acidic Zn species within the Beta zeolite framework[59] and, by extension, the peaks reflecting pyridine adsorption onto Y sites in Y/Beta correspond to Lewis acidic Y sites, as recently suggested elsewhere.[60] The peaks centered at 1545 and 1637 cm^{-1} observed on Y-containing sites are

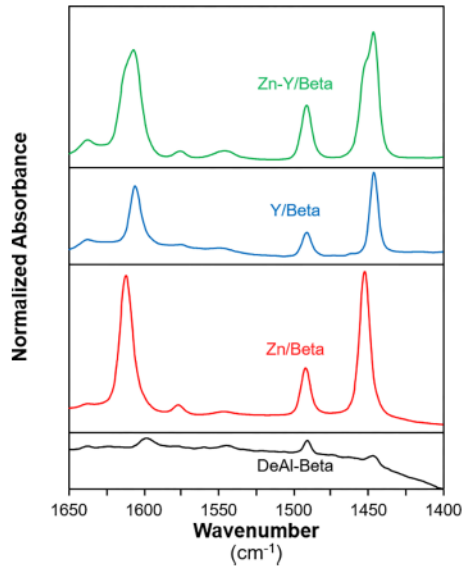

Figure 3. Transmission IR spectra on deAl-Beta and Zn- and Y-containing Beta samples after pyridine saturation at 393 K.

reminiscent of previously assigned peaks for protonated pyridine species[61] derived from interactions with Brønsted acid sites. As these peaks reflecting protonated pyridine are absent from the deAl-Beta parent spectra, these peaks reflect the presence of pyridine-bound Brønsted acidic Y sites on both Y/Beta and Zn–Y/Beta. This would be consistent with Y^{3+} centers embedded within the zeolitic framework that require a nearby proton for charge balance. The spectrum collected on the Zn–Y/Beta sample after pyridine saturation has all six distinct peaks indicative of pyridine adsorbed onto Lewis acidic Zn and Y species and Brønsted acidic Y sites as expected for a sample containing both metals, yet the quantification of distinct Zn and Y active site densities is not possible due to the lack of integrated molar extinction coefficients (integrated peak area ratios and total acid site densities from NH_3–TPD measurements are given in Table S.4 with NH_3–TPD spectra shown in Figure S.8). However, taking these observations together with the XAS analyses, the Zn- and Y-containing Beta zeolites studied here are composed of predominantly site-isolated metal centers despite high metal loadings and consist of Lewis acidic Zn sites and both Lewis and Brønsted acidic Y sites, respectively. Notably, Brønsted acidic Y sites have not been previously reported for Y sites within a zeolitic framework.

This combination of Zn and Y sites on the Beta support is capable of catalyzing ethanol valorization to butadiene and butenes even in low conversion rate measurements (Figure 1), suggesting its catalytic ETB potential at more industrially relevant conversions. High conversion measurements from pseudo-steady-state ethanol conversion over Zn–Y/Beta (3.1 kPa EtOH, balance He, 588 K, WHSV = 0.43 h^{-1}) show 87% ethanol conversion with 60 and 14% selectivities to butadiene and butene isomers (1-butene, *cis*-2-butene, and *trans*-2-butene), respectively, along with smaller concentrations (3–8%) of ethylene, propene, acetaldehyde, diethyl ether, and C_{5+} olefins (product distribution and selectivity given in Figures S.9 and S.10, respectively). Given the high butadiene selectivity, the possibility of using Zn–Y/Beta as a single ETO catalyst for both ETB and subsequent butadiene selective hydrogenation to butene isomers was investigated by cofeeding

https://doi.org/10.1021/acscatal.1c01136
ACS Catal. 2021, 11, 7193–7209

hydrogen. Hydrogen cofeeding with ethanol (0−98.3 kPa H_2, 3.1 kPa EtOH in balance He) does not show discernible differences in either the overall ethanol conversion or the associated product distribution even when the carrier gas is solely composed of hydrogen (Figure S.9). These high conversion measurements suggest that Zn−Y/Beta alone cannot efficiently catalyze the full ETO pathway (Scheme 1) regardless of hydrogen partial pressure, necessitating additional active sites for butadiene selective hydrogenation. These selective hydrogenation active sites must catalyze selective hydrogenation events at hydrogen and butadiene molar ratios, reflecting gas compositions after interactions with Zn−Y/Beta (~1−65 H_2/BD ratio) and ideally maintaining high selective hydrogenation reactivities at stoichiometric H_2/BD ratios, as discussed next using SAA Pt−Cu-supported metal catalysts.

3.2. Multifunctional Catalyst Systems for ETO. Supported metal catalysts consisting of dilute solid solutions of precious metals (e.g., Pt, Pd) within larger domains of transition metal centers (e.g., Cu) have catalytically relevant reactivities for both low-temperature (<423 K) hydrogenation[37,44] and high-temperature (>573 K) dehydrogenation reactions,[62] suggesting that these materials may be relevant butadiene selective hydrogenation catalysts at increased reaction temperatures (>573 K). The selective hydrogenation capabilities of these materials at ETB temperatures (>573 K) are currently unknown though, and potential reaction concerns include butane formation through complete butadiene hydrogenation, minimal hydrogen coverages due to rapid hydrogen desorption at higher temperatures, and limited reactivity at low or stoichiometric H_2/BD ratios. To probe the usefulness of SAA Pt−Cu materials as butadiene selective hydrogenation catalysts within the proposed ETO reaction network (Scheme 1), hydrogen scission barriers, adsorption energies of relevant butadiene, olefin, and hydrogen surface species, and metal d-band centers were calculated from DFT over Cu(111), Pt(111), and Pt−Cu ensemble sites (reflecting a single Pt site replacement into a Cu(111) surface) and are listed in Table 1 (representative DFT images in Figure S.11).

Adsorption energies for all species investigated here are strongest on Pt(111) surfaces and weakest on Cu(111) surfaces. Similar hydrogen adatom adsorption energies onto Cu(111) and SAA Pt−Cu(111) surfaces indicate that hydrogen adatoms formed through hydrogen scission reactions over Pt centers in SAA materials are energetically stabilized to similar extents on both Pt and Cu centers and, given low diffusion barriers to and from neighboring Cu sites, suggest the ready generation of hydrogen islands[37,63] for utilization during hydrogenation reactions. These minimal hydrogen scission barriers are similar (0.05−0.06 eV) on Pt centers in Pt(111) and Pt−Cu(111) ensemble sites, indicating that Pt centers can efficiently catalyze the formation of hydrogen adatom species necessary for most hydrogenation reaction mechanisms regardless of Pt or Cu neighbors.

Table 1. DFT-Calculated Binding Energies (0 K) for Butadiene, Hydrogen, and Butene Isomers onto Pt(111), Cu(111), and SAA Pt−Cu(111) Dilute Solid Solution Surfaces, Hydrogen Scission Barriers, and Pt and Cu d-Band Centers

	Compound	Cu(111)	Pt(111)	SAA Pt−Cu(111)
Binding Energies (eV)	butadiene	−1.27	−2.93	−1.52
	H_2	−0.06	−0.09	−0.06
	H_{adatom}	−0.35	−0.58	−0.38
	1-butene	−0.80	−1.87	−1.21
	cis-2-butene	−0.74	−1.82	−1.17
	trans-2-butene	−0.67	−1.80	−1.13
H_2 Scission Barriers (eV)		0.34	0.05	0.06
Cu d-band Centers (eV)		−2.23		−2.22
Pt d-band Centers (eV)			−2.03	−2.06

Both butadiene and butene isomer adsorption energies decrease with decreasing d-band centers on all three investigated surfaces, as expected for olefin adsorption onto transition metals.[64] Butadiene adsorption is stronger on all catalytic surfaces (by −0.3 to −1.1 eV) than investigated butene surface species, presumably due to favorable binding interactions for both C=C bonds as butadiene adsorbs flat across multiple surface atoms in the absence of other nearby bound molecules (Figure S.11). This adsorption configuration has previously been observed both computationally[44] and through sum frequency generation vibrational spectroscopy measurements.[65] Butadiene adsorption modes oppose those of butene isomers composed of one C=C bond coordinated to surface sites and alkyl chain(s) raised off the surface, effectively yielding decreased butene adsorption strengths relative to butadiene. Adsorption energies indicate more stable adsorption on Pt(111) sites relative to Cu(111) for butadiene, butene isomers, and hydrogen adatoms and are much more pronounced for butadiene (~−1.7 eV) and butene isomers (~−1.1 eV), indicating Pt centers as preferential olefin binding sites. These significantly stronger adsorption interactions may interfere with hydrogen adsorption and scission events over Pt(111) centers despite having minimal hydrogen scission barriers (0.05 eV) relative to those over Cu(111) (0.34 eV). However, Pt sites within the SAA Pt−Cu(111) surface bind butadiene more strongly (by ~−0.4 eV) relative to Cu(111) but more weakly (by ~1.4 eV) relative to Pt(111) without significant changes in hydrogen adsorption strengths and scission barriers, potentially balancing butadiene adsorption with hydrogen adatom formation steps. Taking together the adsorption energies and hydrogen scission barriers, Pt−Cu ensemble sites preferentially adsorb butadiene and butene isomers relative to hydrogen intermediates due to the presence of Pt, limit butadiene adsorption strength through weaker interactions with neighboring Cu atoms relative to Pt neighbors seen on Pt(111), and maintain minimal hydrogen scission barriers, suggesting that Pt−Cu SAA materials may be relevant catalyst candidates for high-temperature (588 K) butadiene selective hydrogenation.

Guided by these computational observations, SAA 0.1Pt6Cu/Al_2O_3 and related supported metal catalysts containing Pt or Cu alone (0.1Pt/Al_2O_3, 2Pt/Al_2O_3, and 6Cu/Al_2O_3) were synthesized via incipient wetness impregnation (IWI) of metal nitrate precursors onto a γ-alumina support for use as catalyst candidates for butadiene selective hydrogenation at relevant ETO conditions. ICP-AES results indicate bulk metal compositions that match nominal IWI solution concentrations on both monometallic materials (0.1% Pt, 1.7% Pt, and 5.5% Cu on 0.1Pt/Al_2O_3, 2Pt/Al_2O_3, and 6Cu/Al_2O_3, respectively) and bimetallic 0.1Pt6Cu/Al_2O_3 (0.1 and 5.9 wt % Pt and Cu, respectively). This equates to a 180:1 Cu/Pt molar ratio on 0.1Pt6Cu/Al_2O_3, indicating the potential for dilute solid solutions of Pt within Cu domains. HAADF-

https://doi.org/10.1021/acscatal.1c01136
ACS Catal. 2021, 11, 7193−7209

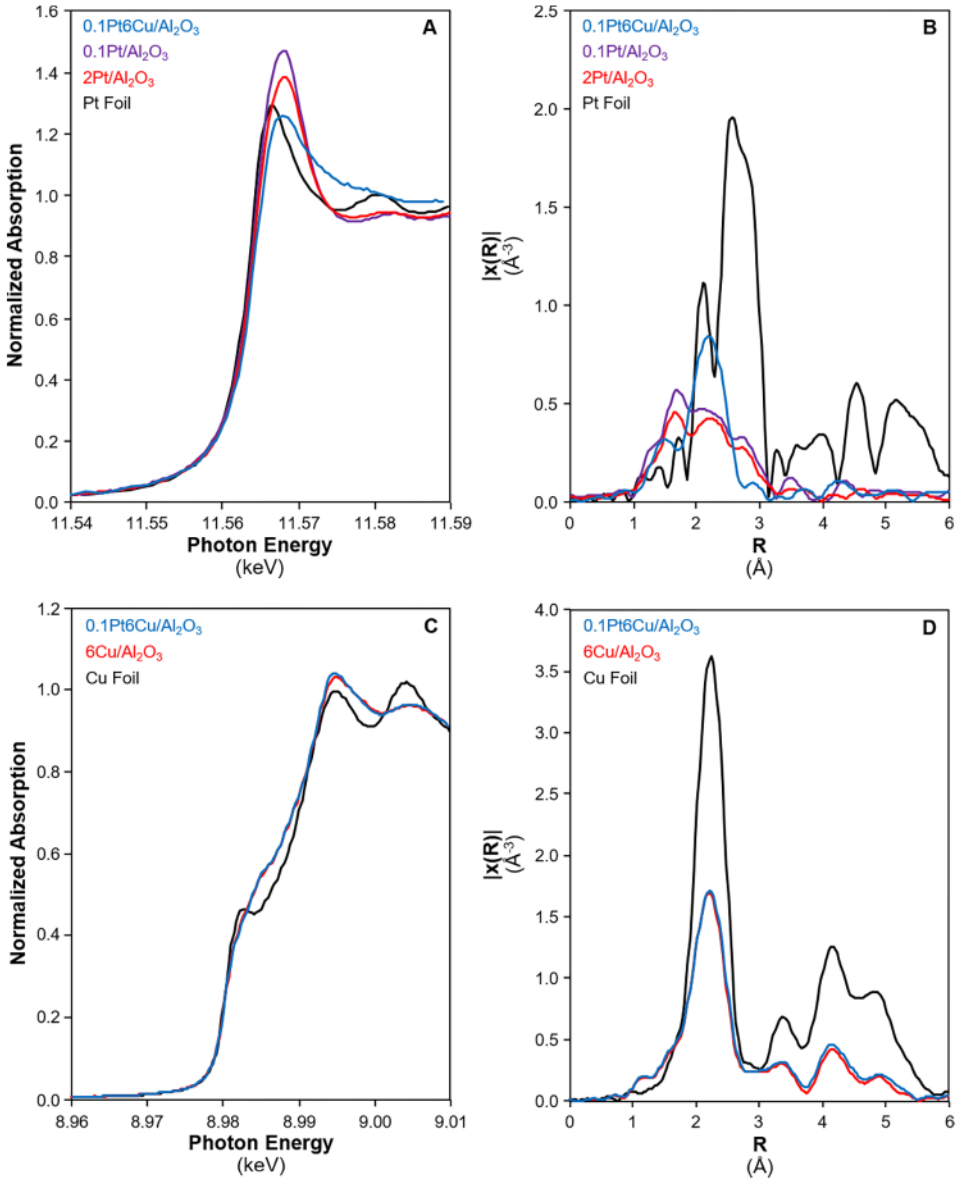

Figure 4. XANES and EXAFS spectra including Pt L_3 edge XANES (A) and EXAFS (B, k^2 weightings) spectra and Cu K edge XANES (C) and EXAFS (D, k^2 weightings) collected on Pt- and Cu-containing supported metal samples. Samples were pretreated at 673 K (5 K min^{-1}) in flowing H_2 and then cooled to room temperature in He prior to collecting XAS spectra.

STEM measurements show primarily isolated Pt centers scattered throughout Cu domains, but Pt nanoparticles are not observed (Figure S.12), suggesting the intimate mixing of Pt and Cu species. In contrast, HAADF-STEM images of $0.1Pt/Al_2O_3$ and $2Pt/Al_2O_3$ show both isolated Pt centers and Pt nanoparticles with higher Pt loadings correlating with increased densities of Pt nanoparticles. HAADF-STEM images of $0.1Pt6Cu/Al_2O_3$ and $6Cu/Al_2O_3$ suggest similar particle size distributions with average particle sizes of 1−3 nm (Figure S.12).

XAS measurements were performed at the Pt L_3 and Cu K edges to characterize the local structures of Pt and Cu in these materials, as seen in Figure 4. XANES edge energies, coordination numbers, and EXAFS fitting parameters for Pt- and Cu-containing materials are listed in Tables S.5 and S.6 and Figures S.13−S.17. XANES spectra collected at the Pt L_3 edge on $0.1Pt6Cu/Al_2O_3$ after reduction at 673 K show a 0.4 eV edge energy increase over Pt foil and a concomitant decrease in white line intensity, consistent with platinum alloys. The corresponding EXAFS spectrum collected on $0.1Pt6Cu/Al_2O_3$ shows only a single R space peak, contrasting the 3 R space peaks of the Pt foil reflecting first-shell Pt−Pt scattering. Based on the STEM analysis and the catalyst composition, the spectrum was modeled using a Pt−Cu scattering path. Fitting gives a coordination number of 8 at a bond distance of 2.56 Å (Table S.6). This result shows that the local environment of platinum in $0.1Pt6Cu/Al_2O_3$ consists exclusively of copper. Additionally, the Pt−Cu bond distance is equal to that of the Cu−Cu bond distance in pure copper, which would be expected in a dilute solid solution alloy following Vegard's law. EXAFS fits of the spectra collected on $0.1Pt/Al_2O_3$ and $2Pt/Al_2O_3$ also have unfilled first-coordination spheres with 7.7 and 6.9 Pt neighbors, respectively. Consistent with the small particle sizes suggested by the coordination numbers, the Pt−Pt bond distances in $0.1Pt/Al_2O_3$ and $2Pt/Al_2O_3$ are contracted to 2.70 and 2.68 Å,

https://doi.org/10.1021/acscatal.1c01136
ACS Catal. 2021, 11, 7193−7209

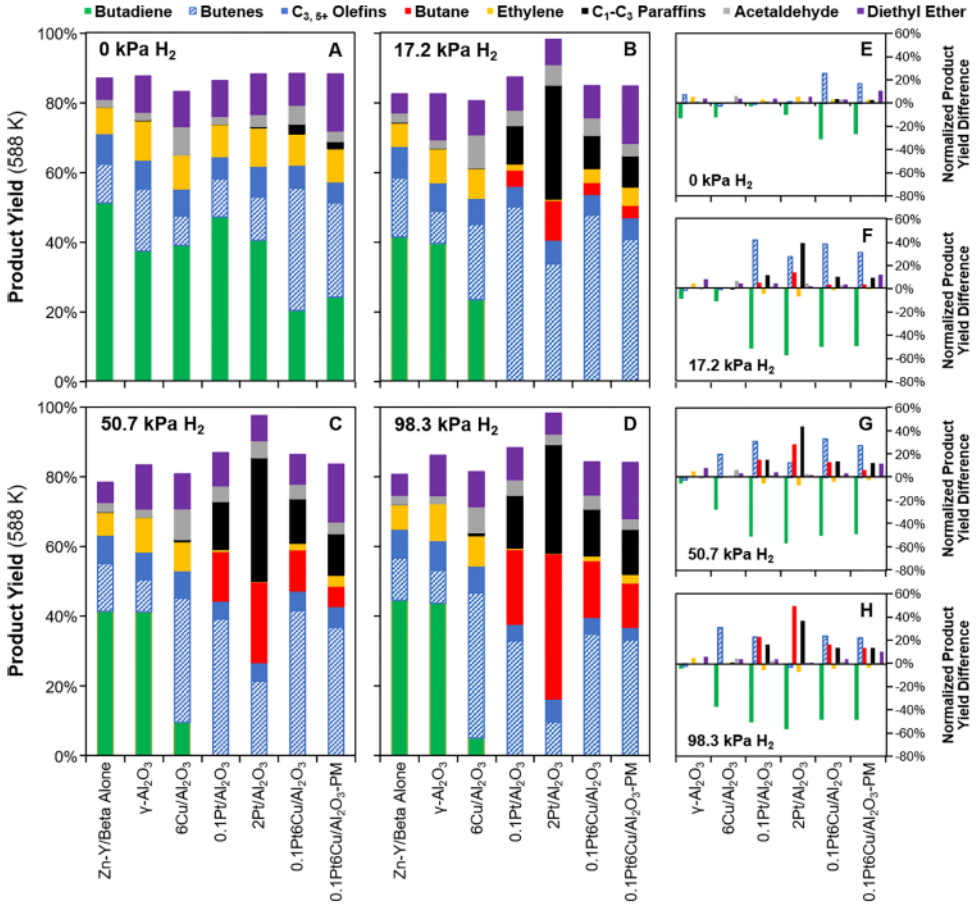

Figure 5. (A–D) Ethanol upgrading product distributions obtained through the two-bed catalytic system composed of Zn–Y/Beta followed by Pt- and/or Cu-containing supported metal catalysts as a function of cofed hydrogen partial pressure at the reactor inlet (3.1 kPa EtOH, 0 (~1 H_2/BD ratio), 17.2 (~12 H_2/BD), 50.7 (~34 H_2/BD), or 98.3 (~65 H_2/BD) kPa H_2 in balance He, 588 K, 0.26 h^{-1} WHSV with respect to the two beds, 0.43 h^{-1} with respect to Zn–Y/Beta alone). Product distributions measured over 0.1Pt6Cu/Al_2O_3-PM reflect a physical mixture of Zn–Y/Beta and 0.1Pt6Cu/Al_2O_3 into a single catalyst bed. Residual product distribution percentages reflect the remaining ethanol at a sub-100% conversion. Errors in product distributions are 15% under these conditions. (E–H) Corresponding differences in observed product yields as a function of secondary catalyst selection at each cofed hydrogen partial pressure. Differences reflect product yield percentages (normalized by ethanol conversion) between each two-bed catalyst setup and the corresponding single-bed product stream over Zn–Y/Beta alone.

respectively, whereas bulk Pt has a Pt–Pt bond distance of 2.77 Å. EXAFS fits (Figures S.16 and S.17) require Pt–O scattering paths on both 0.1Pt/Al_2O_3 and 2Pt/Al_2O_3 (1.99 and 1.97 Å, respectively), indicating a subset of nonreduced Pt sites. Pt–O scattering in the EXAFS is reflected in the XANES as an increase in the edge energy and white line intensity relative to the Pt foil (0.2–0.5 eV) and is suspected to correlate with isolated Pt sites observed in STEM images (Figure S.12) that cannot be readily reduced under the conditions studied here.

XAS measurements collected at the Cu K edge on 0.1Pt6Cu/Al_2O_3 and 6Cu/Al_2O_3 describe the local environment of Cu centers within nanoparticles. Fits of single-shell Cu–Cu scattering paths indicate coordination numbers of 7.3 and 7.2 on 0.1Pt6Cu/Al_2O_3 and 6Cu/Al_2O_3, respectively, and equivalent Cu–Cu bond lengths. This suggests similar metal nanoparticle sizes between the two samples and, by extension, similar bulk surface Cu site distributions. Coordination numbers for Cu (7.3) and Pt (8) on 0.1Pt6Cu/Al_2O_3 are also similar as expected for metal centers evenly distributed throughout occluded nanoparticles. These observations from STEM and XAS suggest the formation of alloyed Pt–Cu nanoparticles with single-site Pt centers distributed within the Cu domains.

The catalytic capabilities of the SAA 0.1Pt6Cu/Al_2O_3 catalyst and the monometallic 0.1Pt/Al_2O_3, 2Pt/Al_2O_3, and 6Cu/Al_2O_3 control materials were studied in conjunction with Zn–Y/Beta for catalyzing the complete ETO reaction network using a layered two-bed setup (Scheme 2), a strategy commonly used to develop multifunctional catalysts for a variety of reactions such as the Fischer–Tropsch synthesis of syngas to liquid fuels[66] or light olefins.[67] Figure 5 depicts ethanol conversions and associated product distributions at 0, 17.2, 50.7, and 98.3 kPa of H_2 (3.1 kPa EtOH in balance He, 588 K; more detailed product distributions and product selectivities are shown in Figures S.18–S.29) over the two-bed catalyst system composed of Zn–Y/Beta and a selective hydrogenation catalyst. Figure 5E–H also depicts product yield difference plots normalized by ethanol conversion at each measured hydrogen partial pressure to highlight product distribution differences between each selective hydrogenation catalyst relative to Zn–Y/Beta alone. Here, 17.2 kPa of cofed hydrogen reflects similar hydrogen partial pressures for acetylene selective hydrogenation within steam-cracking product streams[39] and low-temperature (313–383 K)

https://doi.org/10.1021/acscatal.1c01136
ACS Catal. 2021, 11, 7193–7209

butadiene hydrogenation studies over Cu and SAA Pt−Cu catalysts.[37] Product distributions formed at 588 K are composed of a mix of butadiene, butenes (1-butene, *trans*-2-butene, *cis*-2-butene), $C_{3,5+}$ olefins (predominantly propene, pentenes, and hexenes), oxygenates (acetaldehyde and diethyl ether), and other short-chain hydrocarbons (methane, ethane, ethylene, and propane). Ethanol conversions are consistent (above 80%) at all cofed hydrogen partial pressures and are primarily due to interactions between ethanol and Zn−Y/Beta (Figure S.9).

Product distributions measured without cofed hydrogen at 588 K show an ∼3× higher butene yield over SAA 0.1Pt6Cu/Al_2O_3 than over any other selective hydrogenation catalysts without observable butane formation (Figure 5A). Other Pt- and Cu-containing catalysts display minimal differences in butadiene and butene yields under identical conditions, indicating that Pt or Cu species alone possess insufficient selective hydrogenation reactivity without hydrogen cofeeding at ETO temperatures. Therefore, increased butadiene selective hydrogenation over SAA 0.1Pt6Cu/Al_2O_3 reflects increased reactivity catalyzed by alloyed Pt−Cu ensemble sites relative to Pt or Cu sites alone, which cannot be easily overcome by increasing the bulk Pt loading (by 20× on 2Pt/Al_2O_3). This increased reactivity is accomplished at stoichiometric hydrogen concentrations generated *in situ* from ethanol dehydrogenation, indicating the SAA Pt−Cu catalyst's selective hydrogenation efficacy for the targeted ETO pathway (Scheme 2) relative to other Pt- or Cu-containing catalysts studied here.

Further conversion of butadiene to butene isomers was investigated by cofeeding hydrogen. At all three cofed hydrogen partial pressures studied here (17.2, 50.7, and 98.3 kPa), no residual butadiene is observed over any Pt-containing catalysts. Increased butene and subsequent butane yields are derived from butadiene converted over Pt-containing catalysts with saturated butane formation becoming more pronounced with increasing hydrogen partial pressure. Increased saturated butane yield with increasing cofed hydrogen partial pressure occurs simultaneously with decreased ethylene and propene selectivities (Figures S.26−S.29) and increased C_1−C_3 paraffin formation, indicating that the observed hydrogenation reactivity over Pt centers is indiscriminate over the range of short-chain olefin compounds as expected over Pt-containing catalysts. Decreased butane and C_1−C_3 paraffin formation are observed over 0.1Pt6Cu/Al_2O_3 relative to 2Pt/Al_2O_3 (2.3×) even under a 98.3 kPa hydrogen flow, potentially reflecting the decreased butene adsorption strength onto Pt−Cu ensemble sites relative to Pt centers, as indicated in DFT calculations (Table 1). Complete hydrogenation of butadiene to saturated hydrocarbons reduces the desired C_{3+} olefin yield, indicating the need for minimal or no external hydrogen cofeeding (near-stoichiometric H_2/BD molar ratio) at ETO reaction temperatures for maximum C_{3+} olefin recovery.

The role of Pt−Cu ensemble sites can be further investigated by comparing product distributions measured over the SAA 0.1Pt6Cu/Al_2O_3 and 6Cu/Al_2O_3 catalysts. At all hydrogen partial pressures, product distributions measured over 6Cu/Al_2O_3 show no butane formation, while minimal changes in butene formation are observed at low hydrogen partial pressures (0−17.2 kPa) relative to Zn−Y/Beta alone. Residual butadiene conversion over 6Cu/Al_2O_3 increases directly with hydrogen partial pressure to form butene isomers at high hydrogen partial pressures (50.7−98.3 kPa), but complete butadiene conversion is still not observed even at 98.3 kPa hydrogen. Therefore, Pt centers within the Pt−Cu domains are critical for butadiene selective hydrogenation at low hydrogen and butadiene ratios characteristic of ETB outlet streams (∼1.5 kPa each) and are primarily responsible for complete butadiene conversion even at 17.2 kPa of cofed hydrogen, catalyzing the final reaction steps of the ETO pathway (Scheme 2).

The combination of the bimetallic Zn−Y/Beta composed of at least three distinctive active site types with the bimetallic SAA 0.1Pt6Cu/Al_2O_3 catalyst capable of catalyzing high-temperature hydrogenation reaction at near-stoichiometric hydrogen and butadiene partial pressures yields a butene-rich C_{3+} olefin stream. These observations regarding the site and structural properties of both catalysts, as well as the high conversion product distributions, provide significant evidence of the potential industrial viability of the ETO pathway, yielding desirable olefin precursors for applications including jet fuel production. To further probe the reactivities of these hydrogenation catalysts, single-bed butadiene selective hydrogenation kinetic measurements over Pt- and Cu-containing catalysts are combined with DFT calculations to correlate the unique catalytic behavior of alloyed Pt−Cu active site ensembles with the observed product distributions in the two-bed ETO measurements over 0.1Pt6Cu/Al_2O_3 at the near-stoichiometric H_2/BD ratio (Figure 5A).

3.3. Butadiene Selective Hydrogenation over Monometallic and SAA Pt- and Cu-Containing Catalysts. Butadiene hydrogenation rates obtained over SAA 0.1Pt6Cu/Al_2O_3, 0.1Pt/Al_2O_3, 6Cu/Al_2O_3, and 2Pt/Al_2O_3 catalysts were measured at similar hydrogen and butadiene partial pressures to those expected under high conversion ETB operations. With 3.1 kPa ethanol, an ETB reaction pathway with complete ethanol conversion and perfect butadiene formation selectivity generates a maximum of 1.55 kPa each of hydrogen and butadiene (Scheme 1). Steady-state butene formation rates per gram of catalyst (588 K, 1.51 kPa H_2, 1.51 kPa BD, 0.20 kPa CH_4, SV_{total} = 100 $cm^3\ s^{-1}$ (g catalyst)$^{-1}$) over SAA 0.1Pt6Cu/Al_2O_3 are approximately 20×, 3×, and 0.6× higher than rates over 0.1Pt/Al_2O_3, 6Cu/Al_2O_3, and 2Pt/Al_2O_3, respectively (Table S.7), while reaction rates measured on the γ-alumina support alone are not detectable (<10^{-7} mol butenes (g catalyst)$^{-1}$ s^{-1}). Therefore, butadiene selective hydrogenation events are catalyzed by both Cu and Pt sites. These results are consistent with the observations from ETO experiments (Figure 5A), where significantly higher butene formation was observed over SAA without hydrogen cofeeding when compared with 0.1Pt/Al_2O_3 or 6Cu/Al_2O_3. Selective hydrogenation rates (per gram catalyst) over 0.1Pt6Cu/Al_2O_3 are slightly lower than those over 2Pt/Al_2O_3 (∼20× Pt loading) under purer flow conditions established during single-bed kinetic measurements but not during two-bed ETO reaction measurements at stoichiometric H_2/BD ratios. This may suggest that the Cu-free Pt/Al_2O_3 catalysts suffer inhibition caused by other compounds formed over the Zn−Y/Beta bed, which includes water and other oxygenates (Scheme 2).

Steady-state reaction rates measured over 0.1Pt/Al_2O_3 or 6Cu/Al_2O_3 reflect minimum rates per mole of Pt or Cu, respectively, to compare against rates measured over the SAA catalyst. Here, dilute Pt incorporation within Cu domains (∼180:1 mol Cu/mol Pt) is assumed to insignificantly affect Cu active site densities due to similar Cu particle sizes and bulk Cu coordination between 6Cu/Al_2O_3 and 0.1Pt6Cu/Al_2O_3 from Cu edge XAS measurements (Figure 4 and Table S.5).

https://doi.org/10.1021/acscatal.1c01136
ACS Catal. 2021, 11, 7193−7209

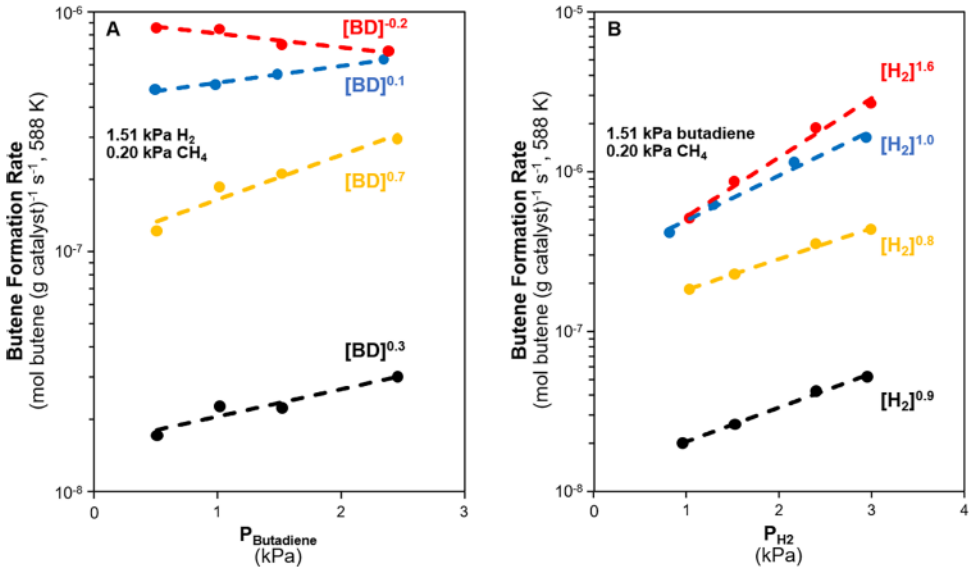

Figure 6. Steady-state combined butene formation rates (588 K, 100 cm^3 s^{-1} (g catalyst)$^{-1}$) collected over 0.1Pt6Cu/Al_2O_3 (blue), 6Cu/Al_2O_3 (orange), 0.1Pt/Al_2O_3 (black), and 2Pt/Al_2O_3 (red) as a function of (A) butadiene partial pressure and (B) hydrogen partial pressure. Dashed lines reflect linear regression best fits.

The linear combination of steady-state rates of the 0.1Pt/Al_2O_3 and 6Cu/Al_2O_3 catalysts remains significantly lower than the rate measured on 0.1Pt6Cu/Al_2O_3 (Table S.7), indicating that Pt−Cu ensemble sites have increased butadiene selective hydrogenation reactivity relative to Cu domains or Pt sites alone at low hydrogen partial pressures.

The kinetic implications of Pt−Cu ensemble sites can be evaluated by comparing the SAA catalyst with the monometallic analogues using apparent reaction orders and DFT-calculated adsorption enthalpies, hydrogen scission barriers, and energy barriers through a commonly utilized Horiuti−Polanyi reaction mechanism for selective hydrogenation.[44] Figure 6 shows steady-state butene formation rates as a function of butadiene and hydrogen partial pressures for the four hydrogenation catalysts studied here (isomer-specific results are given in Figure S.30 and Table S.8). Butene formation rates over both 0.1Pt6Cu/Al_2O_3 and 0.1Pt/Al_2O_3 follow a nearly zero-order dependence on butadiene partial pressure (0.1 and 0.3, respectively), while 2Pt/Al_2O_3 has a lower yet still approximately zero-order dependence (−0.2) and 6Cu/Al_2O_3 has a significantly higher apparent order (0.7). Assuming that butadiene selective hydrogenation follows a Langmuir−Hinshelwood kinetic model over these catalysts as previously modeled over other butadiene selective hydrogenation catalysts (e.g., Pt(111), Pt_2Sn/Pt(111),[68] and Pd/Al_2O_3[69]), differences in apparent butadiene reaction orders most likely reflect different coverages of reactive intermediate species on each catalyst surface. Apparent butadiene reaction orders decrease as calculated butadiene adsorption energies become more negative (Table 1). These adsorption energies indicate that bound butadiene species on kinetically relevant active sites are adsorbed more strongly than hydrogen- or butene-bound surface species and presumably yield higher coverages. Butadiene-covered active sites would corroborate the apparent zero-order butadiene dependence on Pt-containing catalysts where butadiene adsorption is energetically favorable enough to completely saturate kinetically relevant active sites and even becomes inhibitory as seen through the negative apparent reaction order on 2Pt/Al_2O_3. The larger apparent butadiene reaction order over 6Cu/Al_2O_3 relative to Pt-containing catalysts would then reflect a lower coverage on active Cu sites due to 0.25−1.66 eV less favorable butadiene binding enthalpies relative to Pt sites (Table 1). Further, Pt sites embedded within Cu(111) surfaces or Pt(111) also display increased butene adsorption enthalpies relative to Cu sites alone, providing energetically favorable binding sites for butene adsorption and subsequent hydrogenation. The resulting butane formation would increase with hydrogen partial pressure as observed during ETO experiments (>17.2 kPa; Figure 5B−D) over Pt-containing catalysts.

Apparent hydrogen reaction orders are approximately first-order over 0.1Pt6Cu/Al_2O_3 (1.0), 0.1Pt/Al_2O_3 (0.9), and 6Cu/Al_2O_3 (0.8) and considerably higher (1.6) over 2Pt/Al_2O_3. These apparent reaction orders and associated increased butadiene selective hydrogenation rates with increasing hydrogen partial pressure are consistent with the increased butene and butane yields observed in the two-bed system product distributions (Figures 5A−D and S.19−S.22), the largest of which is observed over 2Pt/Al_2O_3. These apparent hydrogen reaction orders trend opposingly with apparent butadiene reaction orders, which may reflect the competitive adsorption of butadiene and hydrogen onto kinetically relevant sites. Further, DFT calculations of Pt centers embedded in both Cu and Pt nanoparticles show ∼0.3 eV lower hydrogen scission barriers than Cu sites alone, indicating essentially barrierless formation of hydrogen adatoms and matching previously reported observations over Pt−Cu SAA materials.[70] These lower hydrogen scission barriers calculated over Pt sites then suggest the formation of bound hydrogen adatom species on either Pt or neighboring Cu centers as previously observed via scanning tunneling microscopy on SAA Pt−Cu materials at 85 K.[37] These hydrogen adatom species would then be capable of facilitating selective hydrogenation reactions with bound butadiene species. Further, these Pt−Cu ensemble sites remain catalytically active significantly longer than isolated Pt sites or small Pt nanoparticles on 0.1Pt/Al_2O_3 (Figure S.31) while limiting inhibitory butadiene interactions seen through the negative

https://doi.org/10.1021/acscatal.1c01136
ACS Catal. 2021, 11, 7193−7209

apparent reaction order (and subsequently the higher hydrogen order) over $2Pt/Al_2O_3$.

Taking the apparent first-order hydrogen reaction orders and nearly zero-order apparent butadiene reaction orders over $0.1Pt6Cu/Al_2O_3$ and $0.1Pt/Al_2O_3$, a Horiuti−Polanyi reaction mechanism can be proposed starting from a bound butadiene intermediate to form 1-butene and *trans*-2-butene, matching previous assertions.[44,71,72] A detailed description is provided in Section S.2.5 and Scheme S.1. Figure 7 shows DFT-calculated energies throughout the investigated reaction mechanism (Scheme S.1) over Cu(111), Pt(111), and SAA Pt−Cu(111) surfaces reflecting $6Cu/Al_2O_3$, $2Pt/Al_2O_3$, and $0.1Pt6Cu/Al_2O_3$ catalysts, respectively[62] (calculated activation energies and energy differences between elementary steps are listed in Table S.9, and butadiene hydrogenation pathways to butane through diradical intermediates (I3 and I4, Scheme S.1) are shown in Figure S.32). The addition of two hydrogen adatoms yields the formation of either butene isomers or two reduced intermediate species (I3 and I4), the latter of which possesses significantly higher energies than 1-butene or *trans*-2-butene and reflects significantly less stable intermediates due to the absence of conjugated bonds. These intermediates must then undergo further hydrogenation to butane prior to desorption from catalytic surfaces or isomerize into more stable butene configurations, the latter of which may consist of significant activation energy barriers that were not investigated here.

After 1-butene or *trans*-2-butene formation, olefin selectivity for butenes relative to butane can be assessed by comparing butene desorption energies with butene hydrogenation activation energy barriers. Over Cu(111) and SAA Pt−Cu(111) surfaces, butene isomer desorption energies are lower than calculated activation energy barriers to form butane (Table S.9), indicating a preference for butene desorption and concomitant termination of the hydrogenation reaction. This difference between desorption energy and butene hydrogenation activation energy is larger over Cu(111) than over SAA Pt−Cu(111). This corroborates observed product distributions from two-bed measurements over $6Cu/Al_2O_3$ and $0.1Pt6Cu/Al_2O_3$, where negligible butane formation is observed over both catalysts at near-stoichiometric H_2/BD ratios but is never observed over $6Cu/Al_2O_3$ at all studied hydrogen partial pressures (Figure 5). The limited difference between butene desorption energy and hydrogenation activation energy over SAA Pt−Cu(111) further corroborates selective butene formation at the near-stoichiometric hydrogen partial pressures in single- or two-bed measurements and could explain the decreased butene selectivity with increasing hydrogen partial pressures given the first-order apparent reaction order with respect to hydrogen partial pressure from experimental measurements (Figure 6). These observations, both experimental and computational, are inconsistent with previously reported calculations indicating that selective hydrogenation reactivities are similar over Cu(111) and Pt−Cu(111) surfaces when accounting for relative surface concentrations of Cu and Pt species.[44] Similar computational observations over Pt(111) indicate that butene hydrogenation activation energy barriers are lower than butene desorption energies (Table S.9). This suggests that hydrocarbon selectivities should heavily favor butane formation over Pt(111), as seen at all cofed hydrogen partial pressures (Figure 5). The above observations on Pt(111) and Cu(111) reflect the potentially highest butane and butene selectivities, respectively, while the reaction energy profile over Pt−Cu(111) contains Pt−Cu active site ensembles possessing both higher hydrogenation reactivity than Cu sites alone and energetic barriers that favor butene desorption over subsequent butene hydrogenation to form butane.

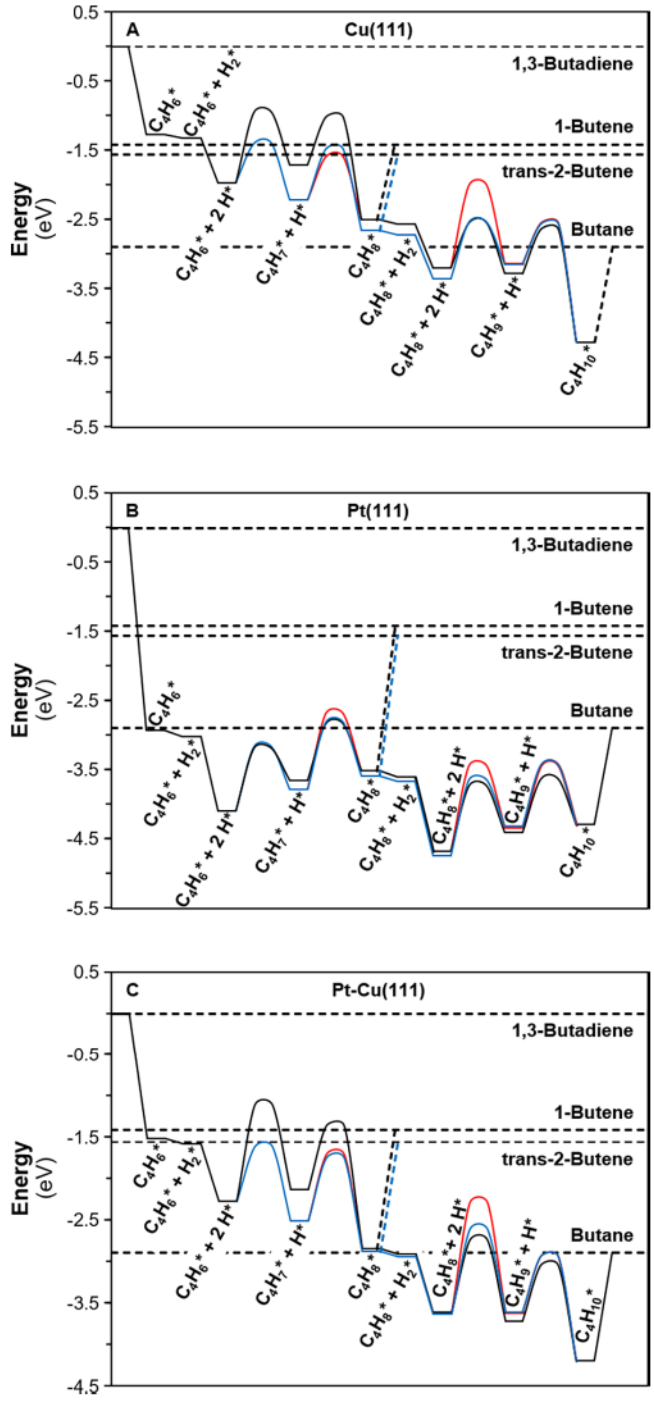

Figure 7. Reaction coordinate diagrams reflecting butadiene selective hydrogenation pathways to form 1-butene and *trans*-2-butene and subsequent butene hydrogenation pathways to form butane over (A) Cu(111), (B) Pt(111), and (C) Pt−Cu(111) surfaces. Distinct pathways are depicted here using the designations presented in Scheme S.1: butadiene → I2 → 1-butene → I6 → butane (black), butadiene → I1 → *trans*-2-butene → I5 → butane (blue), and butadiene → I1 → 1-butene → I5 → butane (red). Diagonal dashed lines reflect desorption energies for bound butenes. Energy differences and activation energies are listed in Table S.9.

https://doi.org/10.1021/acscatal.1c01136
ACS Catal. 2021, 11, 7193−7209

The energy differences between butene desorption and hydrogenation phenomena should be treated generally for comparing these Pt- and Cu-containing catalysts. Increased temperatures will destabilize adsorbed species and decrease desorption energies through entropic contributions, while activation energies will generally be less affected by temperatures for consistent most abundant surface intermediates and kinetically relevant transition states. Therefore, energy differences are maximized at 0 K and will decrease with increasing temperatures, indicating that the selectivity toward butene formation without overhydrogenation to butane should be more pronounced at increased temperatures. The observed trend favoring butene desorption relative to hydrogenation over Cu(111), Pt−Cu(111), and Pt(111) is significantly more obvious with binding energies calculated at reaction temperatures (Table S.9) due to destabilized bound butene intermediates (>1 eV higher binding energies). This trend indicates that the butadiene hydrogenation reaction network should favor butene desorption over further hydrogenation to butane in order of Cu(111), Pt−Cu(111), and Pt(111) with Pt(111) favoring further hydrogenation. This trend should hold at all hydrogen partial pressures as observed in product distributions from two-bed experiments but should shift toward complete butadiene hydrogenation given high hydrogen partial pressures.

Taking the experimental and computational findings together, overall butene formation rates over the Pt−Cu SAA catalyst are higher than those measured over $6Cu/Al_2O_3$ or $0.1Pt/Al_2O_3$ at stoichiometric butadiene and hydrogen partial pressures and are similar to rates over $2Pt/Al_2O_3$ yet with significantly lower Pt metal concentrations. Increased butene formation rates relative to $6Cu/Al_2O_3$ indicate that incorporated Pt centers within Cu domains either generate additional kinetically relevant active sites or shift the overall selective hydrogenation reaction mechanism with an associated higher reactivity. The former may occur by promoting nearby Cu atoms through Cu−H adatom formation due to negligible hydrogen scission barriers over Pt sites. These same Pt sites generate energetically favorable butadiene or butene binding sites while stabilizing butadiene to a far greater extent than butene isomers. In either case, the incorporation of Pt centers into Cu nanoparticle domains within the SAA catalytic material generates active site ensembles capable of catalyzing selective hydrogenation reactions at low relative hydrogen partial pressures with rates that surpass those on monometallic Pt or Cu catalysts. This combination of DFT calculations and apparent kinetic measurements supports the selection of SAA Pt−Cu materials as a critical catalytic component for the final ETO reaction steps, namely, the selective hydrogenation of butadiene at stoichiometric hydrogen and butadiene partial pressures (H_2/BD = 1). While Zn−Y/Beta containing Brønsted acidic Y sites and Lewis acidic Zn and Y sites catalyzes ETB conversion, the selective hydrogenation of butadiene at low hydrogen partial pressures requires Pt−Cu ensemble sites at stoichiometric hydrogen and butadiene partial pressures and ETB-relevant reaction temperatures. However, the applicability of this ETO pathway (achieved over the two-bed composite catalyst of Zn−Y/Beta and SAA $0.1Pt6Cu/Al_2O_3$) must be further demonstrated via optimizing the selectivity of butene-rich C_{3+} olefins.

3.4. Preliminary ETO Reaction Pathway Optimization.

As minimal efforts have been taken here to tune olefin distributions over the composite Zn−Y/Beta and SAA $0.1Pt6Cu/Al_2O_3$ catalyst systems, many opportunities exist to maximize butene and C_{3+} olefin selectivities at high ethanol conversions (e.g., tuning active site distributions, space velocities, and reaction temperatures). Since optimizing product distributions toward specific olefins is not the primary goal of this work as noted by the singular elemental composition of the multifunctional catalyst and the fixed reaction conditions, only a couple of small steps are explored here to enhance the ETO pathway viability. As shown in Figure 5A, ∼20% of the observed product distribution over the composite Zn−Y/Beta and SAA $0.1Pt6Cu/Al_2O_3$ catalyst system (∼88% conversion) is butadiene, indicating that butene yields can be increased simply by balancing butadiene formation with selective hydrogenation reactivity. As expected, increasing the catalyst loading of SAA $0.1Pt6Cu/Al_2O_3$ to equivalent catalyst loadings of Zn−Y/Beta and SAA $0.1Pt6Cu/Al_2O_3$ yields increased butadiene conversion over SAA and selectivity to butenes (54%) and C_{3+} olefins (65%) at slightly higher ethanol conversions (95%; Figure S.33).

Stoichiometric H_2/BD ratios are necessary to avoid overhydrogenation of butadiene to butane, as observed in Figure 5 and DFT energy profile calculations (Figure 7). Positive apparent hydrogen reaction orders over SAA $0.1Pt6Cu/Al_2O_3$ indicate that selective hydrogenation reaction rates can be further increased by increasing hydrogen partial pressures. Increasing the ethanol partial pressure from 3.1 to 6.1 kPa over equivalent Zn−Y/Beta and SAA $0.1Pt6Cu/Al_2O_3$ catalyst loadings maintains a consistent near-stoichiometric H_2/BD ratio while yielding significantly higher butene (65%) and C_{3+} (78%) selectivities at a similar ethanol conversion (94%; Figure S.34). However, these product selectivities remain relatively unoptimized due to no optimization of active site distributions or other reaction conditions responsible for side product formation. Further, these results are expected to hold even when Zn−Y/Beta and $0.1Pt6Cu/Al_2O_3$ are physically mixed into a single bed of composite catalyst based on relatively small changes in nonoptimized product distributions at all studied cofed hydrogen partial pressures (Figure 5; $0.1Pt6Cu/Al_2O_3$-PM).

Despite the need for further catalyst optimization, C_{3+} olefin selectivities observed here at high ethanol conversions (>85%) exceed other published ethanol valorization pathways (Figure S.35 and Table S.11) such as ethanol to olefins via an ethylene intermediate over Brønsted acid zeolites, Guerbet coupling of ethanol and subsequent dehydration to olefin products, and ethanol condensation to form isobutene or propene over oxide materials (e.g., $ZnZrO_x$)[5]. The utility of this two-bed catalytic system is process intensification by performing cascade reactions at a constant temperature and pressure despite the presence of coproducts (e.g., water, oxygenates, ethylene). Further, this two-bed composite Zn−Y/Beta and SAA $0.1Pt6Cu/Al_2O_3$ catalyst setup can operate without cofed hydrogen, a significant advantage from both process design and economic perspectives.

4. CONCLUSIONS

Ethanol valorization to C_{3+} olefin (ETO) is a promising reaction pathway for generating key oligomerization precursors by leveraging butadiene as a critical intermediate. This ETO pathway was investigated over a composite catalyst composed of a bimetallic Zn−Y/Beta zeolite and SAA $0.1Pt6Cu/Al_2O_3$-supported metal catalyst, yielding a high C_{3+} olefin selectivity (78% at 94% ethanol conversion, 588 K) without hydrogen

https://doi.org/10.1021/acscatal.1c01136
ACS Catal. 2021, 11, 7193−7209

cofeeding. XAS measurements and HAADF-STEM images identified the isolated nature of Zn and Y on the Beta zeolite support despite the high Y loading (~7 wt %) and isolated Pt within Cu nanoparticles, while transmission IR spectra collected after pyridine adsorption onto Zn−Y/Beta indicated the presence of both Lewis acidic Zn and Y sites and previously unreported Brønsted acidic Y centers, identifying various active metal species to match with ETO kinetic measurements. Bimetallic Zn−Y/Beta catalyzes the multistep formation of butadiene from ethanol with the concomitant formation of near-stoichiometric hydrogen partial pressures, while SAA 0.1Pt6Cu/Al_2O_3 selectively hydrogenates butadiene to form butene products at this stoichiometric H_2/BD ratio and ETB reaction temperature over Pt−Cu ensemble sites. DFT calculations indicate that increased selective hydrogenation reactivity over Pt−Cu(111) surfaces combines low hydrogen scission barriers and favorable butadiene binding energies with preferential butene desorption energies relative to further hydrogenation activation energies forming butane. Together, this multifunctional catalyst enables direct bioethanol valorization using only *in situ*-generated hydrogen to form butene-rich C_{3+} olefin streams, which are readily oligomerized into longer-chain olefin products necessary for renewable jet fuel production.

■ ASSOCIATED CONTENT

Supporting Information

The Supporting Information is available free of charge at https://pubs.acs.org/doi/10.1021/acscatal.1c01136.

XRD patterns, N_2 adsorption isotherms, XAS fitting details and associated figures, STEM images, NH_3−TPD spectra, additional product distributions and selectivity plots, DFT-calculated adsorption images, additional plots of butene formation rates as a function of butadiene and hydrogen partial pressures, transient butadiene selective hydrogenation profiles, DFT-calculated energy differences and activation energy barriers, additional reaction coordinate diagrams, product distribution plots of preliminary optimization strategies, and comparison of presented ETO pathway relative to literature observations (PDF)

■ AUTHOR INFORMATION

Corresponding Author

Zhenglong Li − *Manufacturing Science Division, Oak Ridge National Laboratory, Oak Ridge, Tennessee 37830, United States;* orcid.org/0000-0001-8811-8625; Email: liz3@ornl.gov

Authors

Michael J. Cordon − *Manufacturing Science Division, Oak Ridge National Laboratory, Oak Ridge, Tennessee 37830, United States*

Junyan Zhang − *Manufacturing Science Division, Oak Ridge National Laboratory, Oak Ridge, Tennessee 37830, United States; Department of Chemical and Biomolecular Engineering, University of Maryland, College Park, Maryland 20742, United States*

Stephen C. Purdy − *Department of Chemical Engineering, Purdue University, West Lafayette, Indiana 47907, United States; Neutron Scattering Division, Oak Ridge National Laboratory, Oak Ridge, Tennessee 37830, United States;* orcid.org/0000-0002-9870-1029

Evan C. Wegener − *Chemical Sciences and Engineering Division, Argonne National Laboratory, Lemont, Illinois 60439, United States*

Kinga A. Unocic − *Center for Nanophase Materials Sciences, Oak Ridge National Laboratory, Oak Ridge, Tennessee 37830, United States*

Lawrence F. Allard − *Material Science and Technology Division, Oak Ridge National Laboratory, Oak Ridge, Tennessee 37830, United States*

Mingxia Zhou − *Materials Science Division, Argonne National Laboratory, Lemont, Illinois 60439, United States;* orcid.org/0000-0002-1896-1024

Rajeev S. Assary − *Materials Science Division, Argonne National Laboratory, Lemont, Illinois 60439, United States;* orcid.org/0000-0002-9571-3307

Jeffrey T. Miller − *Department of Chemical Engineering, Purdue University, West Lafayette, Indiana 47907, United States;* orcid.org/0000-0002-6269-0620

Theodore R. Krause − *Chemical Sciences and Engineering Division, Argonne National Laboratory, Lemont, Illinois 60439, United States*

Fan Lin − *Institute for Integrated Catalysis, Pacific Northwest National Laboratory, Richland, Washington 99354, United States*

Huamin Wang − *Institute for Integrated Catalysis, Pacific Northwest National Laboratory, Richland, Washington 99354, United States;* orcid.org/0000-0002-3036-2649

A. Jeremy Kropf − *Chemical Sciences and Engineering Division, Argonne National Laboratory, Lemont, Illinois 60439, United States*

Ce Yang − *Chemical Sciences and Engineering Division, Argonne National Laboratory, Lemont, Illinois 60439, United States*

Dongxia Liu − *Department of Chemical and Biomolecular Engineering, University of Maryland, College Park, Maryland 20742, United States;* orcid.org/0000-0001-8712-2219

Complete contact information is available at: https://pubs.acs.org/10.1021/acscatal.1c01136

Author Contributions

M.J.C. and J.Z. contributed equally. The manuscript was written through contributions of all authors. All authors have given approval to the final version of the manuscript.

Funding

Microscopy research, K.A.U., M.J.C., J.Z., S.C.P., D.L., and Z.L., were sponsored by the U.S. Department of Energy (DOE), Office of Energy Efficiency and Renewable Energy (EERE), Bioenergy Technologies Office (BETO), under Contract DE-AC05-00OR22725 (ORNL) with UT-Battelle, LLC, and in collaboration with the Chemical Catalysis for Bioenergy (ChemCatBio) Consortium, a member of the Energy Materials Network. Microscopy research was also supported by the Center for Nanophase Materials Sciences (CNMS), which is sponsored by the Scientific User Facilities Division, Office of Basic Energy Sciences, U.S. DOE. MR-CAT operations are supported by the DOE and the MR-CAT member institutions. This research used resources of the Advanced Photon Source, a U.S. DOE Office of Science User Facility operated for the DOE Office of Science by Argonne National Laboratory under Contract No. DE-AC02-

06CH11357. S.C.P. and J.T.M. were supported by the National Science Foundation under Cooperative Agreement No. EEC1647722. The computing resource was provided on "BEBOP", a computing cluster operated by the Laboratory Computing Resource Center at Argonne National Laboratory. M.Z. and R.S.A. acknowledge Computational Chemistry Physics Consortium (CCPC), which is supported by the Bioenergy Technologies Office of Energy Efficiency & Renewable Energy. F.L. and H.W. were financially supported by the U.S. DOE, EERE, Bioenergy Technologies Office, and part of this work was performed at the Pacific Northwest National Laboratory (PNNL), a multiprogram national laboratory operated for DOE by Battelle Memorial Institute. The views and opinions of the authors expressed herein do not necessarily state or reflect those of the U.S. Government or any agency thereof.

Notes

The authors declare the following competing financial interest(s): Patent application is pending for the inventor Z.L. This manuscript has been authored in part by UT-Battelle, LLC, under Contract DE-AC05-00OR22725 with the U.S. Department of Energy (DOE). The U.S. government retains and the publisher, by accepting the article for publication, acknowledges that the U.S. government retains a nonexclusive, paid-up, irrevocable, worldwide license to publish or reproduce the published form of this manuscript, or allow others to do so, for U.S. government purposes. DOE will provide public access to these results of federally sponsored research in accordance with the DOE Public Access Plan (http://energy.gov/downloads/doe-public-access-plan).

■ ACKNOWLEDGMENTS

The authors acknowledge Dr. Meijun Li for additional experimental assistance with the XRD analysis. The authors also thank Shawn K. Reeves and Dr. Qianying Guo for assistance with TEM work.

■ REFERENCES

(1) Renewable Fuels Association. 2019 Ethanol Industry Outlook, 2019.

(2) Iwamoto, M. Selective Catalytic Conversion of Bio-Ethanol to Propene: A Review of Catalysts and Reaction Pathways. *Catal. Today* **2015**, *242*, 243−248.

(3) Sun, J.; Wang, Y. Recent Advances in Catalytic Conversion of Ethanol to Chemicals. *ACS Catal.* **2014**, *4*, 1078−1090.

(4) Adhikari, S. P.; Zhang, J.; Guo, Q.; Unocic, K. A.; Tao, L.; Li, Z. A Hybrid Pathway to Biojet Fuel via 2,3-Butanediol. *Sustainable Energy Fuels* **2020**, *4*, 3904−3914.

(5) Eagan, N. M.; Kumbhalkar, M. D.; Buchanan, J. S.; Dumesic, J. A.; Huber, G. W. Chemistries and Processes for the Conversion of Ethanol into Middle-Distillate Fuels. *Nat. Rev. Chem.* **2019**, *3*, 223−249.

(6) Duan, C.; Zhang, X.; Zhou, R.; Hua, Y.; Chen, J.; Zhang, L. Hydrothermally Synthesized HZSM-5/SAPO-34 Composite Zeolite Catalyst for Ethanol Conversion to Propylene. *Catal. Lett.* **2011**, *141*, 1821−1827.

(7) Tsuchida, T.; Yoshioka, T.; Sakuma, S.; Takeguchi, T.; Ueda, W. Synthesis of Biogasoline from Ethanol over Hydroxyapatite Catalyst. *Ind. Eng. Chem. Res.* **2008**, *47*, 1443−1452.

(8) Bi, J.; Liu, M.; Song, C.; Wang, X.; Guo, X. C-2−C-4 Light Olefins from Bioethanol Catalyzed by Ce-Modified Nanocrystalline HZSM-5 Zeolite Catalysts. *Appl. Catal., B* **2011**, *107*, 68−76.

(9) Sun, J.; Zhu, K.; Gao, F.; Wang, C.; Liu, J.; Peden, C. H. F.; Wang, Y. Direct Conversion of Bio-Ethanol to Isobutene on Nanosized $Zn_xZr_yO_z$ Mixed Oxides with Balanced Acid-Base Sites. *J. Am. Chem. Soc.* **2011**, *133*, 11096−11099.

(10) Zhao, B.; Men, Y.; Zhang, A.; Wang, J.; He, R.; An, W.; Li, S. Influence of Different Precursors on Isobutene Production from Bio-Ethanol over Bifunctional $Zn_1Zr_{10}O_x$ Catalysts. *Appl. Catal., A* **2018**, *558*, 150−160.

(11) Derouane, E. G.; Nagy, J. B.; Dejaifve, P.; Vanhooff, J. H. C.; Spekman, B. P.; Vedrine, J. C.; Naccache, C. Elucidation of Mechanism of Conversion of Methanol and Ethanol to Hydrocarbons on a New Type of Synthetic Zeolite. *J. Catal.* **1978**, *53*, 40−55.

(12) Talukdar, A. K.; Bhattacharyya, K. G.; Sivasanker, S. HZSM-5 Catalysed Conversion of Aqueous Ethanol to Hydrocarbons. *Appl. Catal., A* **1997**, *148*, 357−371.

(13) Galadima, A.; Muraza, O. Zeolite Catalysts in Upgrading of Bioethanol to Fuels Range Hydrocarbons: A Review. *J. Ind. Eng. Chem.* **2015**, *31*, 1−14.

(14) Nakajima, T.; Nameta, H.; Mishima, S.; Matsuzaki, I.; Tanabe, K. A Highly-Active and Highly Selective Oxide Catalyst for the Conversion of Ethanol to Acetone in the Presence of Water-Vapor. *J. Mater. Chem.* **1994**, *4*, 853−858.

(15) Nishiguchi, T.; Matsumoto, T.; Kanai, H.; Utani, K.; Matsumura, Y.; Shen, W. J.; Imamura, S. Catalytic Steam Reforming of Ethanol to Produce Hydrogen and Acetone. *Appl. Catal., A* **2005**, *279*, 273−277.

(16) Hannon, J. R.; Lynd, L. R.; Andrade, O.; Benavides, P. T.; Beckham, G. T.; Biddy, M. J.; Brown, N.; Chagas, M. F.; Davison, B. H.; Foust, T.; Junqueira, T. L.; Laser, M. S.; Li, Z.; Richard, T.; Tao, L.; Tuskan, G. A.; Wang, M.; Woods, J.; Wyman, C. E. Technoeconomic and Life-Cycle Analysis of Single-Step Catalytic Conversion of Wet Ethanol into Fungible Fuel Blendstocks. *Proc. Natl. Acad. Sci. U.S.A.* **2020**, *117*, 12576−12583.

(17) Makshina, E. V.; Dusselier, M.; Janssens, W.; Degreve, J.; Jacobs, P. A.; Sels, B. F. Review of Old Chemistry and New Catalytic Advances in the On-Purpose Synthesis of Butadiene. *Chem. Soc. Rev.* **2014**, *43*, 7917−7953.

(18) Sushkevich, V. L.; Ivanova, I. I. Mechanistic Study of Ethanol Conversion into Butadiene over Silver Promoted Zirconia Catalysts. *Appl. Catal., B* **2017**, *215*, 36−49.

(19) Yan, T.; Dai, W.; Wu, G.; Lang, S.; Hunger, M.; Guan, N.; Li, L. Mechanistic Insights into One-Step Catalytic Conversion of Ethanol to Butadiene over Bifunctional Zn-Y/Beta Zeolite. *ACS Catal.* **2018**, *8*, 2760−2773.

(20) Müller, P.; Burt, S. P.; Love, A. M.; McDermott, W. P.; Wolf, P.; Hermans, I. Mechanistic Study on the Lewis Acid Catalyzed Synthesis of 1,3-Butadiene over Ta-BEA Using Modulated Operando DRIFTS-MS. *ACS Catal.* **2016**, *6*, 6823−6832.

(21) Foley, B. L.; Johnson, B. A.; Bhan, A. Kinetic Evaluation of Deactivation Pathways in Methanol-to-Hydrocarbon Catalysis on HZSM-5 with Formaldehyde, Olefinic, Dieneic, and Aromatic Co-Feeds. *ACS Catal.* **2021**, *11*, 3628−3637.

(22) Albright, L. F.; Marek, J. C. Mechanistic Model for Formation of Coke in Pyrolysis Units Producing Ethylene. *Ind. Eng. Chem. Res.* **1988**, *27*, 755−759.

(23) Nguyen, N. T. T.; Matei-Rutkovska, F.; Huchede, M.; Jaillardon, K.; Qingyi, G.; Michel, C.; Millet, J. M. M. Production of 1,3-Butadiene in One Step Catalytic Dehydration of 2,3-Butanediol. *Catal. Today* **2019**, *323*, 62−68.

(24) Wu, J.; Peng, Z.; Sun, P.; Bell, A. T. N-Butane Dehydrogenation over Pt/Mg(In)(Al)O. *Appl. Catal., A* **2014**, *470*, 208−214.

(25) Larina, O. V.; Kyriienko, I. P.; Batakin, D. Y.; Vorokhta, M.; Khalakhan, I.; Nychiporuk, Y. M.; Matolin, V.; Soloviev, S. O.; Orlyk, S. M. Effect of ZnO on Acid-Base Properties and Catalytic Performances of ZnO/ZrO_2-SiO_2 Catalysts in 1,3-Butadiene Production from Ethanol-Water Mixture. *Catal. Sci. Technol.* **2019**, *9*, 3964−3978.

(26) Da Ros, S.; Jones, M. D.; Mattia, D.; Pinto, J. C.; Schwaab, M.; Noronha, F. B.; Kondrat, S. A.; Clarke, T. C.; Taylor, S. H. Ethanol to 1,3-Butadiene Conversion by Using ZrZn-Containing MgO/SiO_2

https://doi.org/10.1021/acscatal.1c01136
ACS Catal. 2021, 11, 7193−7209

Systems Prepared by Co-Precipitation and Effect of Catalyst Acidity Modification. *ChemCatChem* **2016**, *8*, 2376−2386.
(27) Zhu, Q.; Wang, B.; Tan, T. Conversion of Ethanol and Acetaldehyde to Butadiene over MgO-SiO_2 Catalysts: Effect of Reaction Parameters and Interaction between MgO and SiO_2 on Catalytic Performance. *ACS Sustainable Chem. Eng.* **2017**, *5*, 722−733.
(28) Sushkevich, V. L.; Ivanova, I. I.; Ordomsky, V. V.; Taarning, E. Design of a Metal-Promoted Oxide Catalyst for the Selective Synthesis of Butadiene from Ethanol. *ChemSusChem* **2014**, *7*, 2527−2536.
(29) Angelici, C.; Meirer, F.; van der Eerden, A. M. J.; Schaink, H. L.; Goryachev, A.; Hofmann, J. P.; Hensen, E. J. M.; Weckhuysen, B. M.; Bruijnincx, P. C. A. Ex Situ and Operando Studies on the Role of Copper in Cu-Promoted SiO_2-MgO Catalysts for the Lebedev Ethanol-to-Butadiene Process. *ACS Catal.* **2015**, *5*, 6005−6015.
(30) Shylesh, S.; Gokhale, A. A.; Scown, C. D.; Kim, D.; Ho, C. R.; Bell, A. T. From Sugars to Wheels: The Conversion of Ethanol to 1,3-Butadiene over Metal-Promoted Magnesia-Silicate Catalysts. *ChemSusChem* **2016**, *9*, 1462−1472.
(31) Janssens, W.; Makshina, E. V.; Vanelderen, P.; De Clippel, F.; Houthoofd, K.; Kerkhofs, S.; Martens, J. A.; Jacobs, P. A.; Sels, B. F. Ternary Ag/MgO-SiO_2 Catalysts for the Conversion of Ethanol into Butadiene. *ChemSusChem* **2015**, *8*, 994−1008.
(32) Dastillung, R.; Cadran, N.; Jacquin, M.; Huyghe, R.; Fischer, B. Process for Producing 1,3-Butadiene from a Feedstock Comprising Ethanol. U.S. Patent US9776933B22013.
(33) Sushkevich, V. L.; Ivanova, I. I. Ag-Promoted ZrBEA Zeolites Obtained by Post-Synthetic Modification for Conversion of Ethanol to Butadiene. *ChemSusChem* **2016**, *9*, 2216−2225.
(34) Kyriienko, P. I.; Larina, O. V.; Soloviev, S. O.; Orlyk, S. M.; Calers, C.; Dzwigaj, S. Ethanol Conversion into 1,3-Butadiene by the Lebedev Method over MTaSiBEA Zeolites (M = Ag, Cu, Zn). *ACS Sustainable Chem. Eng.* **2017**, *5*, 2075−2083.
(35) Wang, C.; Zheng, M.; Li, X.; Li, X.; Zhang, T. Catalytic Conversion of Ethanol into Butadiene over High Performance LiZnHf-MFI Zeolite Nanosheets. *Green Chem.* **2019**, *21*, 1006−1010.
(36) Dai, W.; Zhang, S.; Yu, Z.; Yan, T.; Wu, G.; Guan, N.; Li, L. Zeolite Structural Confinement Effects Enhance One-Pot Catalytic Conversion of Ethanol to Butadiene. *ACS Catal.* **2017**, *7*, 3703−3706.
(37) Lucci, F. R.; Liu, J.; Marcinkowski, M. D.; Yang, M.; Allard, L. F.; Flytzani-Stephanopoulos, M.; Sykes, E. C. H. Selective Hydrogenation of 1,3-Butadiene on Platinum-Copper Alloys at the Single-Atom Limit. *Nat. Commun.* **2015**, *6*, No. 8550.
(38) Hu, C.; Sun, J.; Wang, D.; Peng, M.; Shao, M.; Zhu, Q.; Ma, D. Hydrogen Diffusion Guided Design of Pt-Based Alloys for Inhibition of Butadiene Over-Hydrogenation. *ChemPhysChem* **2019**, *20*, 1804−1811.
(39) Godínez, C.; Cabanes, A. L.; Villora, G. Experimental Study of the Selective Hydrogenation of Steam Cracking C-2 Cut. Front End and Tail End Variants. *Chem. Eng. Commun.* **1998**, *164*, 225−247.
(40) Koeppel, R. A.; Wehrli, J. T.; Wainwright, M. S.; Trimm, D. L.; Cant, N. W. Selective Hydrogenation of C-4-Alkynes over a Copper on Silica Catalyst. *Appl. Catal., A* **1994**, *120*, 163−177.
(41) Pattamakomsan, K.; Suriye, K.; Dokjampa, S.; Mongkolsiri, N.; Praserthdam, P.; Panpranot, J. Effect of Mixed Al_2O_3 Structure between Theta- and Alpha-Al_2O_3 on the Properties of Pd/Al_2O_3 in the Selective Hydrogenation of 1,3-Butadiene. *Catal. Commun.* **2010**, *11*, 311−316.
(42) Lonergan, W. W.; Xing, X.; Zheng, R.; Qi, S.; Huang, B.; Chen, J. G. Low-Temperature 1,3-Butadiene Hydrogenation over Supported Pt/3d/Gamma-Al_2O_3 Bimetallic Catalysts. *Catal. Today* **2011**, *160*, 61−69.
(43) Liu, J.; Shan, J.; Lucci, F. R.; Cao, S.; Sykes, E. C. H.; Flytzani-Stephanopoulos, M. Palladium-Gold Single Atom Alloy Catalysts for Liquid Phase Selective Hydrogenation of 1-Hexyne. *Catal. Sci. Technol.* **2017**, *7*, 4276−4284.
(44) Yang, K.; Yang, B. Identification of the Active and Selective Sites over a Single Pt Atom-Alloyed Cu Catalyst for the Hydrogenation of 1,3-Butadiene: A Combined DFT and Microkinetic Modeling Study. *J. Phys. Chem. C* **2018**, *122*, 10883−10891.
(45) Harris, J. W.; Cordon, M. J.; Di Iorio, J. R.; Vega-Vila, J. C.; Ribeiro, F. H.; Gounder, R. Titration and Quantification of Open and Closed Lewis Acid Sites in Sn-Beta Zeolites That Catalyze Glucose Isomerization. *J. Catal.* **2016**, *335*, 141−154.
(46) Kresse, G.; Hafner, J. Ab-Initio Molecular-Dynamics Simulation of the Liquid-Metal Amorphous-Semiconductor Transition in Germanium. *Phys. Rev. B* **1994**, *49*, No. 14251.
(47) Kresse, G.; Furthmuller, J. Efficiency of Ab-Initio Total Energy Calculations for Metals and Semiconductors Using a Plane-Wave Basis Set. *Comput. Mater. Sci.* **1996**, *6*, 15−50.
(48) Grimme, S.; Antony, J.; Ehrlich, S.; Krieg, H. A Consistent and Accurate Ab Initio Parametrization of Density Functional Dispersion Correction (DFT-D) for the 94 Elements H-Pu. *J. Chem. Phys.* **2010**, *132*, No. 154104.
(49) Grimme, S.; Ehrlich, S.; Goerigk, L. Effect of the Damping Function in Dispersion Corrected Density Functional Theory. *J. Comput. Chem.* **2011**, *32*, 1456−1465.
(50) Perdew, J. P.; Burke, K.; Ernzerhof, M. Generalized Gradient Approximation Made Simple. *Phys. Rev. Lett.* **1996**, *77*, No. 3865.
(51) Henry, C. R. Morphology of Supported Nanoparticles. *Prog. Surf. Sci.* **2005**, *80*, 92−116.
(52) Methfessel, M.; Paxton, A. T. High-Precision Sampling for Brillouin-Zone Integration in Metals. *Phys. Rev. B* **1989**, *40*, No. 3616.
(53) Henkelman, G.; Uberuaga, B. P.; Jonsson, H. A Climbing Image Nudged Elastic Band Method for Finding Saddle Points and Minimum Energy Paths. *J. Chem. Phys.* **2000**, *113*, 9901−9904.
(54) Henkelman, G.; Jonsson, H. A Dimer Method for Finding Saddle Points on High Dimensional Potential Surfaces Using Only First Derivatives. *J. Chem. Phys.* **1999**, *111*, 7010−7022.
(55) Hölderich, W. F.; Tjoe, J. Direct Hydrogenation of Aromatic Carboxylic Acids to Their Corresponding Aldehydes with Zinc Oxide Catalysts. *Appl. Catal., A* **1999**, *184*, 257−264.
(56) Keshavaraja, A.; Hegde, V. R.; Pandey, B.; Ramaswswamy, A. V.; Kumar, P.; Ravindranathan, T. An Yttrium-Based Strong Lewis-Acid for the Heterogeneous Catalysis of the Diels-Alder Reaction. *Angew. Chem., Int. Ed.* **1995**, *34*, 2143−2145.
(57) Palomino, G. T.; Pascual, J. J. C.; Delgado, M. R.; Parra, J. B.; Arean, C. O. FT-IR Studies on the Acidity of Gallium-Substituted Mesoporous MCM-41 Silica. *Mater. Chem. Phys.* **2004**, *85*, 145−150.
(58) Connell, G.; Dumesic, J. A. The Generation of Bronsted and Lewis Acid Sites on the Surface of Silica by Addition of Dopant Cations. *J. Catal.* **1987**, *105*, 285−298.
(59) Orazov, M.; Davis, M. E. Catalysis by Framework Zinc in Silica-Based Molecular Sieves. *Chem. Sci.* **2016**, *7*, 2264−2274.
(60) Qi, L.; Zhang, Y.; Conrad, M. A.; Russell, C. K.; Miller, J.; Bell, A. T. Ethanol Conversion to Butadiene over Isolated Zinc and Yttrium Sites Grafted onto Dealuminated Beta Zeolite. *J. Am. Chem. Soc.* **2020**, *142*, 14674−14687.
(61) Hussein, G. A. M.; Gates, B. C. Surface and Catalytic Properties of Yttrium Oxide: Evidence from Infrared Spectroscopy. *J. Catal.* **1998**, *176*, 395−404.
(62) Sun, G.; Zhao, Z.-J.; Mu, R.; Zha, S.; Li, L.; Chen, S.; Zang, K.; Luo, J.; Li, Z.; Purdy, S. C.; Kropf, A. J.; Miller, J. T.; Zeng, L.; Gong, J. Breaking the Scaling Relationship via Thermally Stable Pt/Cu Single Atom Alloys for Catalytic Dehydrogenation. *Nat. Commun.* **2018**, *9*, No. 4454.
(63) Boucher, M. B.; Zugic, B.; Cladaras, G.; Kammert, J.; Marcinkowski, M. D.; Lawton, T. J.; Sykes, E. C. H.; Flytzani-Stephanopoulos, M. Single Atom Alloy Surface Analogs in $Pd_{0.18}Cu_{15}$ Nanoparticles for Selective Hydrogenation Reactions. *Phys. Chem. Chem. Phys.* **2013**, *15*, 12187−12196.
(64) Norskov, J. K.; Abild-Pedersen, F.; Studt, F.; Bligaard, T. Density Functional Theory in Surface Chemistry and Catalysis. *Proc. Natl. Acad. Sci. U.S.A.* **2011**, *108*, 937−943.
(65) Krier, J. M.; Michalak, W. D.; Cai, X.; Carl, L.; Komvopoulos, K.; Somorjai, G. A. Sum Frequency Generation Vibrational Spectroscopy of 1,3-Butadiene Hydrogenation on 4 nm Pt@SiO_2,

https://doi.org/10.1021/acscatal.1c01136
ACS Catal. 2021, 11, 7193−7209

Pd@SiO_2, and Rh@SiO_2 Core-Shell Catalysts. *Nano Lett.* **2015**, *15*, 39−44.
(66) Sartipi, S.; Makkee, M.; Kapteijn, F.; Gascon, J. Catalysis Engineering of Bifunctional Solids for the One-Step Synthesis of Liquid Fuels from Syngas: A Review. *Catal. Sci. Technol.* **2014**, *4*, 893−907.
(67) Jiao, F.; Li, J.; Pan, X.; Xiao, J.; Li, H.; Ma, H.; Wei, M.; Pan, Y.; Zhou, Z.; Li, M.; Miao, S.; Li, J.; Zhu, Y.; Xiao, D.; He, T.; Yang, J.; Qi, F.; Fu, Q.; Bao, X. Selective Conversion of Syngas to Light Olefins. *Science* **2016**, *351*, 1065−1068.
(68) Gautier, S.; Sautet, P. Coadsorption of Butadiene and Hydrogen on the (111) Surfaces of Pt and Pt_2Sn Surface Alloy: Understanding the Cohabitation from First-Principles Calculations. *J. Phys. Chem. C* **2017**, *121*, 25152−25163.
(69) Alves, J. A.; Bressa, S. P.; Martinez, O. M.; Barreto, G. F. Kinetic Study of the Selective Catalytic Hydrogenation of 1,3-Butadiene in a Mixture of n-Butenes. *J. Ind. Eng. Chem.* **2012**, *18*, 1353−1365.
(70) Fu, Q.; Luo, Y. Catalytic Activity of Single Transition-Metal Atom Doped in Cu(111) Surface for Heterogeneous Hydrogenation. *J. Phys. Chem. C* **2013**, *117*, 14618−14624.
(71) Yan, H.; Lv, H.; Yi, H.; Liu, W.; Xia, Y.; Huang, X.; Huang, W.; Wei, S.; Wu, X.; Lu, J. Understanding the Underlying Mechanism of Improved Selectivity in Pd(1) Single-Atom Catalyzed Hydrogenation Reaction. *J. Catal.* **2018**, *366*, 70−79.
(72) Feng, Y.; Zhou, L.; Wan, Q.; Lin, S.; Guo, H. Selective Hydrogenation of 1,3-Butadiene Catalyzed by a Single Pd Atom Anchored on Graphene: The Importance of Dynamics. *Chem. Sci.* **2018**, *9*, 5890−5896.

https://doi.org/10.1021/acscatal.1c01136
ACS Catal. 2021, 11, 7193−7209